JACS
JOURNAL OF THE AMERICAN CHEMICAL SOCIETY
pubs.acs.org/JACS
Article

Operando Heating and Cooling Electrochemical 4D-STEM Probing Nanoscale Dynamics at Solid–Liquid Interfaces

Sungin Kim,[#] Valentin Briega-Martos,[#] Shikai Liu, Kwanghwi Je, Chuqiao Shi, Katherine Marusak Stephens, Steven E. Zeltmann, Zhijing Zhang, Rafael Guzman-Soriano, Wenqi Li, Jiahong Jiang, Juhyung Choi, Yafet J. Negash, Franklin S. Walden, II, Nelson L. Marthe, Jr., Patrick S. Wellborn, Yaofeng Guo, John Damiano, Yimo Han, Erik H. Thiede, and Yao Yang*

Cite This: https://doi.org/10.1021/jacs.5c05005

ABSTRACT: *Operando*/*in situ* methods have revolutionized our fundamental understanding of molecular and structural changes at solid–liquid interfaces and enabled the vision of "watching chemistry in action". *Operando* transmission electron microscopy (TEM) emerges as a powerful tool to interrogate time-resolved nanoscale dynamics, which involve local electrical fields and charge transfer kinetics distinctly different from those of their bulk counterparts. Despite early reports on electrochemical or heating liquid-cell TEM, developing *operando* TEM with simultaneous electrochemical and thermal control remains a formidable challenge. Here, we developed *operando* heating and cooling electrochemical liquid-cell scanning TEM (EC-STEM). By integrating a three-electrode electrochemical circuit and an additional two-electrode thermal circuit, we can investigate heterogeneous electrochemical kinetics across a wide temperature range of −50 to 300 °C. We used Cu electrodeposition/stripping processes as a model system to demonstrate quantitative electrochemistry from −40 to 95 °C in both transient and steady states in aqueous and organic solutions, which paves the way for investigating energy materials operating in extreme climates. Machine learning-assisted quantitative 4D-STEM structural analysis in cold liquids (−40 °C) reveals a distinct two-stage growth of nanometer-scale mossy Cu nanoislands with random orientations followed by μm-scale Cu dendrites with preferential orientations. This work benchmarked electrochemistry in the three-electrode EC-STEM and systematically investigated the temperature and pH dependence of the Pt pseudoreference electrode (RE). At room temperature, the Pt pseudo-RE shows a reliable potential of 0.8 ± 0.1 V vs the standard hydrogen electrode and remains pH-independent on the reversible hydrogen electrode scale. We anticipate that *operando* heating/cooling EC-STEM will become invaluable for understanding fundamental temperature-controlled nanoscale electrochemistry and advancing renewable energy technologies (e.g., catalysts and batteries) in realistic climates.

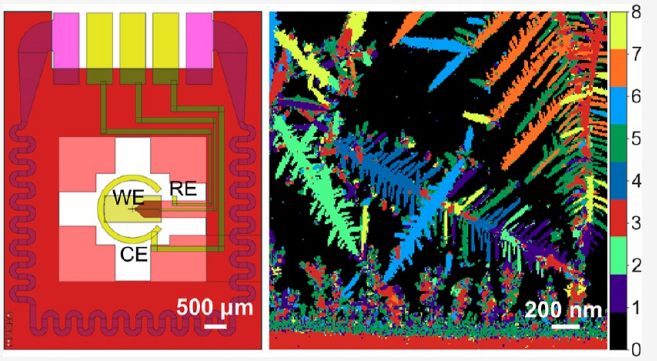

INTRODUCTION

Temperature is the most ubiquitous parameter in tuning chemical reaction rates in modern laboratories[1,2] among a range of environmental stimuli including pressure,[3] light,[4] electrical bias,[5] magnetic field,[6] or mechanical force[7] accessible to chemists and material scientists. The empirical observation of a 2–3-fold increase in the reaction rate for every 10 °C increase in temperature[2] helped chemists develop the first semi-quantitative understanding of chemical kinetics and is often demonstrated in classical iodine clock reactions taught in undergraduate chemistry laboratories.[8] Over the past century, studies of temperature effects have guided the vast development of solution-based organic and inorganic chemistry at elevated temperatures. The exponential temperature dependence of chemical reaction rates was described in the Arrhenius equation as early as the 19th century,[9] which was later elaborated in the transition-state theory and serves as the cornerstone of understanding thermodynamics and kinetics in physical chemistry.[10] Temperature has been explored as the primary tool to tune reaction rates in organic and colloidal synthesis[11] from room temperature to around 300 °C and thermal catalysis at higher temperatures in chemical industry, such as Haber–Bosch ammonia synthesis, steam methane reforming, and Fischer–Tropsch synthesis, among others.[12−14] However, the

Received: March 24, 2025
Revised: May 13, 2025
Accepted: May 14, 2025

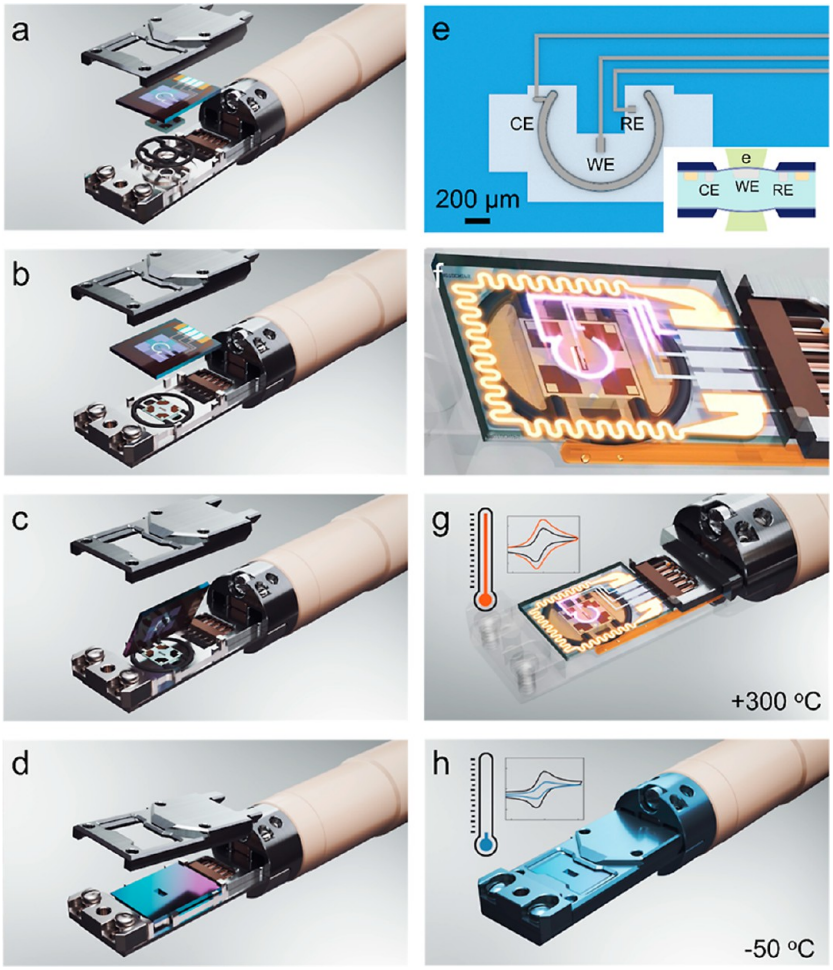

Figure 1. Schematic of *operando* heating and cooling EC-STEM. (a–d) The assembly process of a liquid-cell holder with a large electrochemical chip forms a liquid pocket with the small chip inserted in the gasket and later covered by Ti lead. (e,f) The design of a five-electrode circuit with a three-electrode electrochemical circuit (WE, CE, and RE) and a two-electrode heating/cooling circuit. Inset in (e): the cross-sectioned view of the liquid cell with bulged SiN_x windows in high vacuum. (g,h) Schematic of *operando* heating/cooling EC-STEM with CV profiles under high and low temperatures, respectively.

temperature effects on electrochemistry are less explored until recently due to emerging interests in renewable energy applications.[15] The deployment of hydrogen energy relies on key technologies including proton and anion exchange membrane fuel cells (PEMFCs and AEMFCs) and water electrolyzer-based clean H_2 production, which operate at elevated temperatures of 60–90 °C.[16−19] The higher temperature not only enhances catalyst kinetics but also poses a significant challenge to the durability of electrocatalysts, which are subjected to various temperature-dependent degradation mechanisms (Ostwald ripening, coalescence, dissolution, nanoparticle detachment from a catalyst support, etc.)[20] The rapid-growing electric vehicle (EV) industry requires the development of safe and fast-charging lithium-ion batteries, which face a real-world challenge under both cold and hot climates (−40 to 60 °C).[21] In particular, battery operation at low temperatures is necessary for EVs to operate in cold weather[22] and electronics developed for space missions (the Mars Rover requires a battery operating temperature of −40 to 40 °C).[23] For instance, a cold climate could lead to 40% decrease in the driving range of EVs and it remains a significant challenge to charge EVs below freezing temperatures.[24] While a mild temperature range of 30–60 °C has been shown to improve battery cycling performance, an extreme temperature above 60 °C will lead to the thermal decomposition of the battery materials and possibly catastrophic failure.[25,26] All those applications point out the need to develop *operando*/*in situ* diagnostic methods to probe nanoscale electrochemical kinetics under controlled temperatures.[27,28]

In situ (on site/in position in Latin) methods enable monitoring of real-time changes under reaction-relevant conditions, while *ex situ* (off site in Latin) measurements are performed on pristine or post-mortem samples.[28] *In situ* measurements often deviate from optimal operating conditions, such as environmental transmission electron microscopy (TEM) at low pressure to simulate gas-phase catalytic reactions at high pressure. *Operando* (operating/working in Latin) methods measure operating catalysts under experimental conditions comparable to those of benchtop experiments. The term "*operando*" was proposed by Bañares, Weckhuysen, and others in the early 2000s as an alternative for "*in situ*" Raman spectroscopy to emphasize the importance of simultaneous spectroscopic and activity measurements under catalytic reaction conditions.[29,30] In the context of electrochemistry, *operando* refers to analytical methods that can deliver comparable reaction rates (electrochemical currents) at comparable driving forces (applied potentials) relative to

https://doi.org/10.1021/jacs.5c05005
J. Am. Chem. Soc. XXXX, XXX, XXX−XXX

benchtop experiments. We also acknowledge that the gap between "*in situ*" and "*operando*" can be minimized by increasing the complexity of instrumental design to simulate a working device or catalytic reactor and enable simultaneous activity measurements and/or reaction product detection. *Operando*/*in situ* electrochemical liquid-cell scanning/transmission electron microscopy (EC-S/TEM) has emerged as an important method to track time-resolved nanoscale structural and compositional changes under real-time reaction conditions.[28] Over the past decades, *operando* EC-S/TEM has been developed and employed in understanding electrochemical processes including metal electrodeposition,[31,32] dynamic evolution of electrocatalysts,[33−37] and battery cycling,[38−42] among many other applications.[28] To date, *operando* EC-S/TEM has demonstrated quantitative electrochemistry while acquiring quantitative S/TEM imaging, diffraction, and spectroscopy at nanometer-to-atomic scales.[27,35] On the other hand, *operando*/*in situ* heating liquid-cell TEM has been used to study bubble formation,[43] nanocrystal growth/etching,[44−47] and polymer self-assembly processes[48] at elevated temperatures. However, it remains a longstanding technical challenge to enable simultaneous electrochemical and temperature control in crowded microchips embedded in a confined liquid space. Recently, Ross and coworkers customized a two-electrode electrochemical chip with a heating circuit and investigated electrochemical Ni etching at room temperature and 50 °C.[49] In this work, we developed *operando* heating and cooling EC-STEM with a three-electrode electrochemical circuit and a two-electrode heating/cooling circuit to achieve quantitative electrochemistry with access to a full temperature range of −50 to 300 °C. *Operando* electrochemical four-dimensional (4D) STEM studies of Cu electrodeposition and stripping processes serve as a model system to investigate heterogeneous nucleation and growth mechanisms, since Cu electrodeposition is widely used for fabricating electrical interconnects of integrated circuits in the semiconductor industry.[50] This study has a broad impact on metal electrodeposition at solid−liquid interfaces, which have important technological applications, such as metal electroplating, corrosion protection, and preparation of electrocatalysts.[51] Temperature- and potential-dependent electrochemical kinetics were investigated in both aqueous and organic solutions. A rigorous analysis of temperature and pH dependence of the reference electrode (RE) potentials has been conducted to evaluate the three-electrode electrochemistry with a Pt pseudo-RE, a critically important yet poorly understood component in the three-electrode EC-STEM. We anticipate that this newly developed *operando* heating/cooling EC-STEM will stimulate the wide use of *operando* TEM in electrochemical studies of energy materials.

RESULTS AND DISCUSSIONS

The central component of *operando* heating and cooling EC-STEM is an electrochemical liquid cell with a heating circuit, which is compatible with high vacuum conditions of TEM and enables quantitative electrochemical and temperature control in liquid environments (Figure 1). The electrochemical liquid cell is composed of a liquid pocket sealed by a large electrochemical chip and a small chip, as depicted in the liquid cell assembly process (Figure 1a and Video S1). The small chip is first inserted in the perfluoroelastomer gasket-style O-ring, which prevents the liquid from leaking outside the O-ring. The small chip has a 50 nm spacer and etched trenches on four corners to facilitate the liquid flow near the nanochannel and rapidly replenish fresh electrolytes[27] (Figures 1b and S1). The large chip is patterned with five electrodes and has a 500 nm spacer (Figure 1b), which is placed facing down the small chip after aligning the thin silicon nitride (SiN_x) view windows (550 × 40 μm) on both large and small chips (Figure 1c,d). The resulting liquid cell has a nominal liquid thickness of 550 nm and will experience a significant bulging process of the two 50 nm thick SiN_x windows due to the pressure differential between the liquid cell and the vacuum in the TEM column (~10^{-6} Pa, Figure 1e, inset and Figure S1). The window bulging will lead to a practical liquid thickness of 500−1000 nm or greater at the WE,[52] making it very challenging to perform high-resolution EC-STEM imaging, diffraction, or spectroscopy. This issue will be addressed later with a thin liquid layer created by reversibly electrogenerated hydrogen bubbles under electrochemical conditions.

The design of a five-electrode system with a three-electrode electrochemical circuit and a two-electrode heating/cooling circuit is the key innovation of this work (Figure 1e,f). The Si-based microchip has dimensions of 6 × 4.5 × 300 μm (length × width × thickness) and is patterned with five electrodes by lithography processes. The electrochemical circuit includes a three-electrode design, which has a working electrode (WE) and reference electrode (RE) surrounded by the counter electrode (CE) (Figure 1e). The WE has a dimension of 130 × 20 μm, which is made of Pt (~50 nm thick) with a Ti adhesion layer (~25 nm) or low-contrast glassy carbon (~60 nm thick). In this work, we employed the Pt WE chip for Cu electrodeposition, while the electrochemically inert glassy carbon WE is better suited for studying nanocatalysts.[35,53] The circular Pt CE allows a radially symmetric electric field around the WE. The Pt CE has a significantly larger electrode area of ~0.3 mm^2, which enables rapid polarization and sustains the high current density required by the WE. The RE is also made of Pt (75 × 75 μm) and relies on the redox couple of surface Pt oxide formed on the Pt film (PtO_x/Pt), i.e., a Pt pseudo-RE which will be discussed in depth in Figures 6 and 7. A two-electrode heating/cooling circuit (tungsten coil) is fabricated around the three-electrode electrochemical circuit (Figure 1f). Given the distance between the two circuits is less than 100 μm, tremendous efforts in electrical engineering have been devoted to minimizing the "cross-talk" between them as the heating/cooling circuit requires a mA-level current to control the temperature of the large thermal mass of microchips and liquids, while the electrochemical circuit demands the high-accuracy detection of a pA-level current. Another important feature to assess is the thermal homogeneity across the entire view window and electrode areas under controlled temperatures. An infrared camera, used to measure the temperatures at four corners of the SiN_x window, showed that the electrochemical chip under heating conditions could achieve the target temperatures across a wide temperature range from 50 to 300 °C with a relative error of 1−2 °C (Figure S2 and Table S1). The electrochemical chip under cooling conditions has demonstrated a high accuracy of temperature measurements from room temperature down to a temperature of −78 °C with a relative error of less than 1 °C (Figure S3 and Table S2). *Operando* heating EC-STEM can achieve *operando* electrochemical measurements in hot liquids from room temperature up to 300 °C by controlling the electric current passing through the heating circuit (Figure 1g). With the same setup, *operando* cooling EC-STEM can demonstrate reliable electrochemical measurements in cold liquids from room temperature down to −50 °C by heat exchange through a thermally conductive rod connecting the sample tip to a

https://doi.org/10.1021/jacs.5c05005
J. Am. Chem. Soc. XXXX, XXX, XXX−XXX

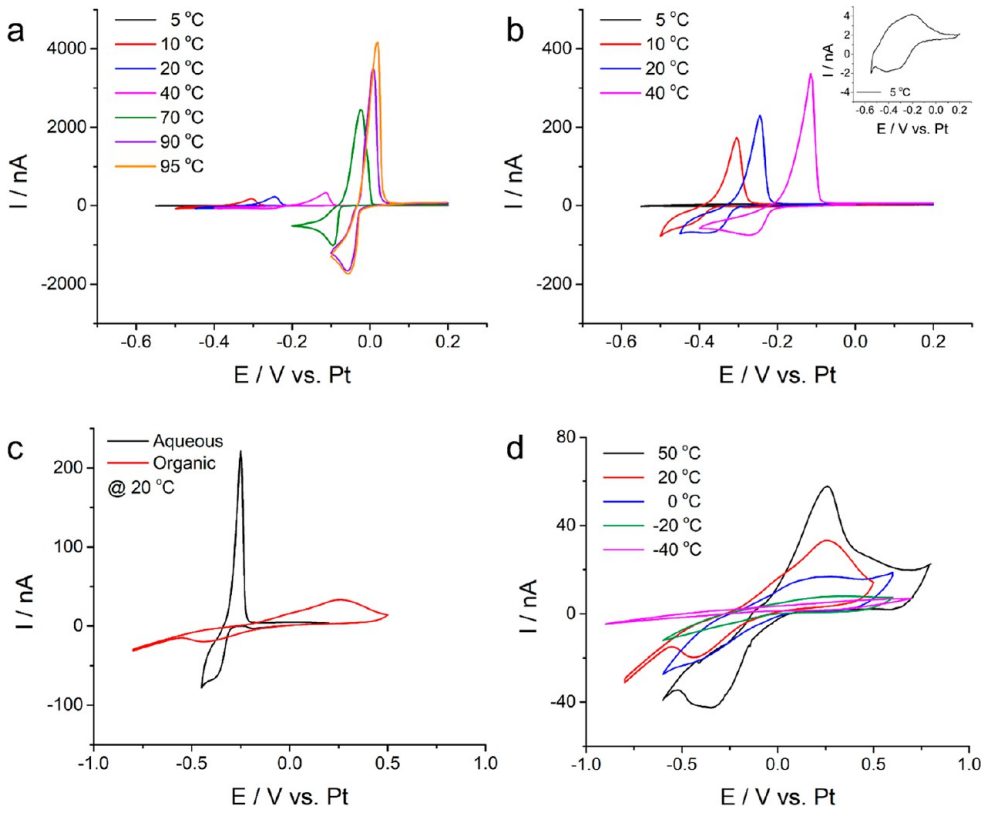

Figure 2. Temperature-dependent Cu electrodeposition/stripping processes in the EC-STEM setup. (a,b) CV profiles in an aqueous solution (10 mM $CuSO_4$ + 0.1 M H_2SO_4) at 50 mV/s under various controlled temperatures of 5 to 95 °C. The inset shows the CV profile acquired at 5 °C with a redox current of less than 4 nA. (c) CV profiles in an aqueous solution (10 mM $CuSO_4$ + 0.1 M H_2SO_4) and organic solution (10 mM $Cu(OAc)_2$ in H_2O/ethanol (v. 1:1)) at 50 mV/s under the same temperature of 20 °C. (d) CV profiles in the organic solution across a temperature range of −40 to 50 °C at 50 mV/s.

thermoelectric Peltier cooler. The "cold side" of the thermoelectric Peltier can get down as low as −76 °C while the "hot side" is kept at temperatures closer to room temperature by using circulated water from an attached water chiller (Figure 1h, see experimental section for details). Cyclic voltammetry (CV) profiles in Figure 1g,h resemble the enhanced and suppressed electrochemical kinetics under heating and cooling conditions, respectively (currents in CV are qualitative and not drawn to the scale). Videos S2 and S3 provide a live illustration of the capability of *operando* heating/cooling EC-STEM to reveal electrochemical kinetics in liquid across a wide temperature range from −50 to 300 °C.

Cu electrodeposition and stripping processes were selected as the model system to investigate temperature-dependent heterogeneous electrochemical kinetics. CV experiments were performed to investigate Cu electrodeposition/stripping (reduction/oxidation) processes in a transient (non-steady) state (Figure 2). CV profiles were acquired in an aqueous solution (10 mM $CuSO_4$ and 0.1 M H_2SO_4) with a pH of ∼1 at 50 mV/s across a wide temperature range of 5 to 95 °C approaching the freezing/boiling points of H_2O, respectively (Figure 2a,b). The upper potential limit was set at 0.2 V vs Pt RE to ensure complete stripping (oxidation) processes, while the lower potential limit was set to achieve full electrodeposition (reduction) processes at −0.4 to −0.5 V at temperatures below 40 °C, −0.2 V at 70 °C, and −0.1 V at temperatures above 90 °C. As the temperature increased from 20 to 95 °C, the Cu electrodeposition current increased from around −70 to −1750 nA, while the stripping current increased from about ∼230 to 4200 nA, which shows an approximately 20-fold increase in the redox current, indicating a significant increase in electrochemical reaction kinetics at elevated temperatures (Figure 2a). It should be noted that the ∼18-fold increase in the deposition peak current from 20 to 95 °C is slightly smaller than that for the stripping peak current (∼25-fold). This asymmetry is attributed to the influence of the temperature-dependent mass transport on the Cu deposition process, while the Cu stripping current does not depend on this factor and follows a classical Butler−Volmer response until the deposited Cu is depleted from the surface.[54] The reduction/oxidation peak potential difference is ∼120 mV at 20 °C, which suggests that Cu electrodeposition/stripping is an irreversible two-electron process. In electrochemistry, a reaction is considered reversible if the electron transfers are fast and the system follows the Nernst equation. A reversible one-electron process has a theoretical anodic/cathodic peak potential difference of 57 mV at 25 °C, while a reversible two-electron process has a theoretical value of 35 mV at 95 °C ($\Delta E_p = 2.2\frac{RT}{nF}$, where R, T, n, and F are the ideal gas constant, temperature, electron transfer number, and Faraday constant, respectively).[54] The redox peak difference decreased from ∼120 mV at 20 °C to ∼70 mV at 95 °C, approaching the theoretical value of 35 mV, which suggests an enhanced electrochemical reaction reversibility at elevated temperatures between cathodic (reduction) and anodic (oxidation) processes at elevated temperatures.

As the temperature decreased from 20 to 5 °C, the Cu stripping current decreased drastically from ∼230 to ∼4 nA (Figure 2b, inset), which suggests severely suppressed electrochemical kinetics as the temperature approaches the freezing

https://doi.org/10.1021/jacs.5c05005
J. Am. Chem. Soc. XXXX, XXX, XXX−XXX

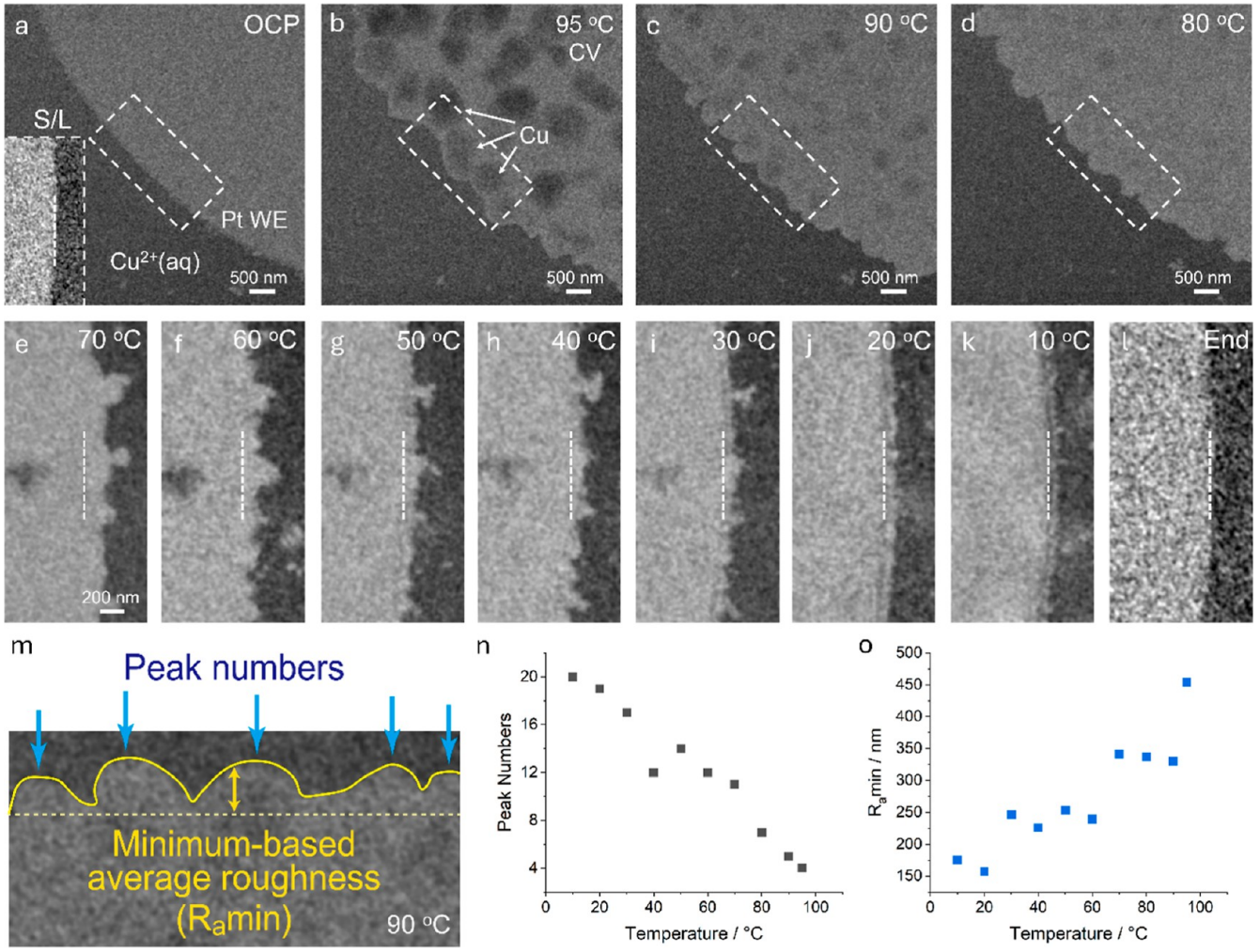

Figure 3. *Operando* heating/cooling EC-STEM of Cu electrodeposition/stripping processes during transient-state CV cycles in the aqueous solution at 50 mV/s. (a) STEM image at the OCP at room temperature. The inset is extracted from the dashed box with the dashed line marking the solid/liquid (S/L) interfaces. (b–d) EC-STEM images of electrodeposited Cu at the maximum amount of growth under temperatures of 95, 90, and 80 °C, respectively. The STEM imaging contrast reversal at 95 °C is due to very thick Cu films. (e–k) *Operando* EC-STEM images of electrodeposited Cu during CV cycles under temperatures of 70 to 10 °C with an interval of 10 °C. The dashed line marks the position of the electrode–electrolyte interface at the OCP. (l) The clean S/L interface at the end of all ten CV experiments under temperatures from 95 to 5 °C, when compared to the pristine interface in the (a) inset, suggests no beam damage during CV cycles. (m) A graphical illustration for the peak numbers and $R_a$min. (n,o) Temperature-dependent (n) peak numbers and (o) $R_a$min.

point of 0 °C. The 3-order-of-magnitude increase in redox currents from 5 to 70 °C was primarily assigned to enhanced reaction kinetics since the ionic conductivity of $CuSO_4$ solutions only increased by about two times across a similar temperature range (Table S3). CV profiles among five consecutive cycles show well-overlapped features at 20 °C and highly reproducible features at elevated temperatures (80 °C), demonstrating that the *operando* heating/cooling EC-STEM setup is capable of delivering reproducible electrochemical behaviors over extended periods of time (Figure S4).

Operando EC-STEM images directly visualize heterogeneous Cu electrodeposition/stripping processes at the nanometer scale (Figure 3). At the open-circuit potential (OCP), the solid (Pt electrode) and liquid (aqueous electrolyte) interfaces were directly visualized in *operando* EC-STEM images (Figure 3a). The inset of Figure 3a exhibits the solid–liquid (S/L) interface as marked by the dashed line. Figure 3b–k exhibits the maximum amount of Cu electrodeposited on the Pt WE, which occurs when the electrodeposition peak is complete in the anodic scan (e.g., −0.3 V for CV at 20 °C, Figure 2b). At 20 °C, Cu exhibited a planar growth with a relatively uniform Cu deposition layer (~100 nm, Figure 3j) when compared to the S/L interface in the bare Pt WE (Figure 3a, inset). As the temperature increased from 20 to 50 °C, Cu grew steadily thicker films with nanoislands formed due to heterogeneous electrical fields at the S/L interface (Figure 3g–j), which was ascribed to kinetic roughening followed by diffusion-limited growth in previous *operando* TEM studies of Cu electrodeposition.[55,56] From 50 to 70 °C, the Cu film further grew with a thickness reaching ~200 nm and an increase in the surface roughness (Figure 3e–g). As the temperature further increased from 80 to 95 °C, dramatic growth of Cu grains occurred throughout the entire Pt WE (Figure 3b–d). As the EC-STEM image is acquired in high-angle annular dark-field (HAADF) mode, the HAADF-STEM image contrast is readily interpretable and sensitive to heavy elements since the image intensity, I, is proportional to atomic density, N, and atomic number, Z ($I \propto N \cdot Z^{1.7}$).[57] At higher temperatures, the brightness of the STEM

https://doi.org/10.1021/jacs.5c05005
J. Am. Chem. Soc. XXXX, XXX, XXX–XXX

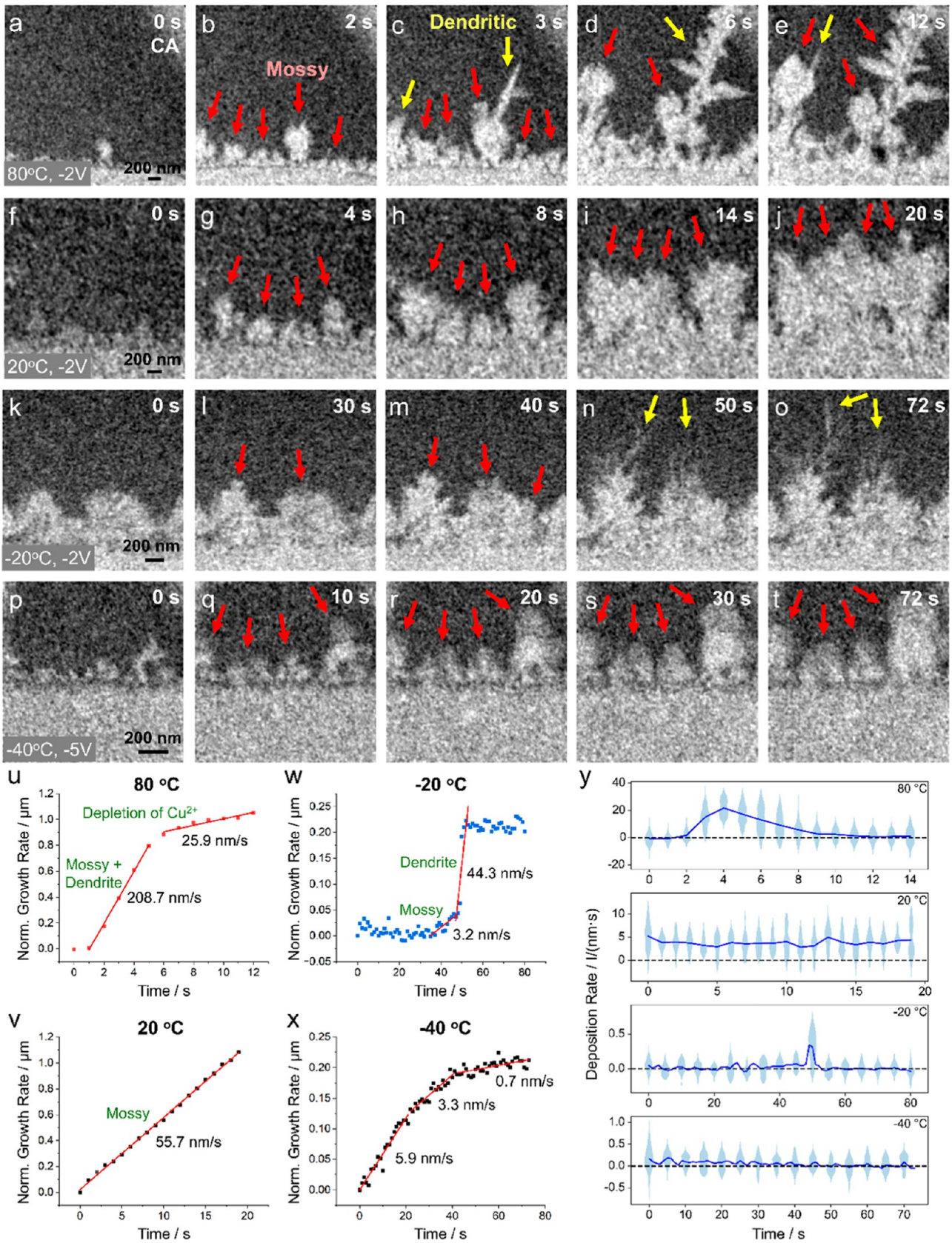

Figure 4. *Operando* heating/cooling EC-STEM of Cu deposition under steady-state CA experiments in the organic solution at (a−e) 80 °C, (f−j) 20 °C, and (k−o) −20 °C under −2 V vs Pt and (p−t) −40 °C under CA of −5 V vs Pt. (u−x) Normalized growth rates (nm/s) of deposited Cu measured at (u) 80 °C, (v) 20 °C, (w) −20 °C, and (x) −40 °C. (y) Violin plots of 2D distribution of growth rates I/(nm·s^2) of individual EC-STEM frames at 80, 20, −20, and −40 °C. Blue lines are mean values of the growth rates.

https://doi.org/10.1021/jacs.5c05005
J. Am. Chem. Soc. XXXX, XXX, XXX−XXX

imaging progressively increases, and a larger area is covered by Cu samples (Figure 3d−j), which are consistent with a gradually increasing amount of electrodeposited Cu. However, at 90 and 95 °C, STEM imaging contrast of Cu grains appears darker (Figure 3b,c), suggesting a contrast reversal in the HAADF-STEM image due to the Cu layer being thicker than 500 nm so that it scatters electrons outside of the outer angle of the HAADF detector and leads to a lower STEM imaging contrast.[58,59] *Operando* EC-STEM movies at 95 °C and CV cycles were simultaneously tracked and are visualized in Video S4.

As the temperature dropped from 20 to 10 °C (Figure 3j,k), the electrodeposited Cu film decreased from ∼100 to ∼70 nm. At a temperature of 5 °C, the Cu electrodeposition was completely quenched with no observable Cu growth (Figure S5), which is consistent with a significant decay of the Cu electrodeposition peak current from −80 nA at 10 °C to less than −2 nA at 5 °C (Figure 2b). At the end of all 10 CV experiments, the S/L interface exhibits a clean Pt WE surface (Figure 3l), which is nearly identical with that at the OCP (Figure 3a, inset), suggesting no observable beam damage. The beam dose control experiment shows no beam damage of 10 mM $CuSO_4$ at a beam voltage of 300 keV and a beam dose of around 1.5 e/(nm^2·s) after a total exposure time of ∼1500 s (Figure S6).

To quantify temperature effects on heterogeneous Cu domains, we analyzed peak numbers and minimum-based average roughness ($R_a$min), which correspond to the number and the size of nuclei, respectively (Figure 3m). $R_a$min is the average deviation of the surface profile in relation to its minimum line.[60] As the temperature increased from 10 to 95 °C, peak numbers decreased from 20 to 4, while the $R_a$min increased from ∼150 to ∼450 nm (Figure 3n,o). This finding indicates that increasing temperature leads to a fewer number of nuclei with enlarged grain sizes under non-steady-state CV conditions. This observation is consistent with the classical nucleation theory and previous studies in which an elevated temperature leads to a decrease in the overpotential, resulting in an increased nucleus radius and a lower nucleation density.[61,62] This quantitative analysis demonstrates the reliability and applicability of our newly developed *operando* heating/cooling EC-STEM that enables us to reveal temperature-dependent nanoscale electrochemical kinetics.

To investigate electrochemical kinetics in cold liquids at temperatures way below 0 °C through our *operando* cooling EC-STEM, an organic solution is required to maintain a liquid form as low as −40 °C while sustaining ionic conductivity for Cu electrodeposition/stripping processes. 10 mM copper(II) acetate ($Cu(OAc)_2$) was dissolved in a water/ethanol mixture with a volume ratio of 1:1 to form an organic solution, which has the same bulk concentration of Cu^{2+} as 10 mM $CuSO_4$ in an aqueous solution. The CV profile in organic solution at 20 °C exhibits a much more sluggish electrodeposition/stripping process with a stripping current of ∼33 nA, when compared with that in the aqueous solution (∼230 nA) at 20 °C (Figure 2c). In addition, the reduction/oxidation peak potential difference in the organic solution is ∼700 mV, which is considerably larger than that in the aqueous solution (∼120 mV), revealing a much more irreversible electrochemical reaction in the organic solution, relative to the aqueous solution. CV profiles in organic solutions at various temperatures are presented in Figure 2d. As the temperature decreased from 50 to 20 and 0 °C, the stripping peak current decreased from 58 to 33 and 17 nA, respectively, suggesting a slower reaction kinetics in organic solutions at lower temperatures (Figure 2d). As the temperature decreases to −20 and −40 °C, the Cu electrodeposition and stripping peaks diminish and eventually disappear, leading to nearly pure capacitive behaviors without redox couples at −40 °C. The electrochemical potential window in the organic solution was expanded considerably due to the suppressed proton activity.[63] While the hydrogen evolution reaction (HER) generates H_2 bubbles in the aqueous solution at around −0.8 V vs Pt (∼0 V vs RHE), the HER in the organic solution occurs at a much more negative potential of around −2 V vs Pt. The suppressed proton activity in the organic solution presents an opportunity to explore electrochemical kinetics in the organic solution under very negative potentials. In light of negligible morphological changes during CV cycles in the organic solution, more aggressive electrochemical experiments were designed to be performed under constant potentials (i.e., chronoamperometry (CA)). CA at −2 V delivered a stable electrodeposition (reduction) current at −200 nA at 20 °C, which increased to around −800 nA at 50 °C and around −1200 nA at 80 °C (Figure S7a). As the temperature decreased to −20 °C, the CA at −2 V reached a much lower current of −34 nA (Figure S7b). As the temperature reached a low level at −40 °C, a minimal current of around −20 nA was achieved with the CA at an aggressive potential of −5 V (Figure S7b). Overall, CA profiles show strong temperature-dependent Cu electrodeposition kinetics.

Operando EC-STEM movies were acquired for the quantitative evolution of the temperature-dependent structural evolution of Cu under steady-state CA conditions with constant driving forces (Figure 4). Across a wide temperature range (80 to −40 °C), Cu exhibited diffusion-controlled growth behaviors including mossy and dendritic growth, which is likely due to the low diffusion rate of Cu^{2+} in the organic solution under large overpotentials.[64] At 80 °C, Cu electrodeposition started with mossy growth (Figure 4a,b) and abruptly switched to dendritic growth with the formation of side branches at 3 s (Figure 4c), which are marked by red and yellow arrows, respectively. All *operando* EC-STEM images were denoised with Gaussian blur to improve STEM image contrast (Figure S8). Quantitative analysis reveals its rapid growth up to the initial 6 s with growth rates exceeding 200 nm/s (Figure 4d,u). The growth rate (nm/s) was calculated by normalizing the growth rate of the sample area (nm^2/s) to the field of view (nm). During this period, both mossy and dendritic growth occurred simultaneously (Figure 4c,d), which suggests that the local deposition environment is spatially nonuniform. Heterogeneity in electrodeposited Cu surfaces can cause variations in the local electric fields. Enhanced fields at protruding surfaces and elevated temperatures accelerate Cu electrodeposition kinetics, leading to the rapid depletion of Cu^{2+} at the surface, which results in a dendritic growth. At the same time, elevated temperatures lead to enhanced diffusion and a sufficient supply of Cu^{2+} to the growth front, prompting Cu electrodeposition to follow mossy growth instead of dendritic growth. The rapid growth of the dendrite led to nonuniform roughness of the growth front (Figure S9), which is often detrimental in practical applications involving metal electrodeposition.[65] A similar dendritic growth was also observed at a CA of −2 V at an intermediate elevated temperature at 50 °C (Figure S10). Subsequently, the growth rate reduced drastically to less than 30 nm/s (Figures 4d,e,u, S11, and Video S5), which is attributed to the rapid consumption of Cu^{2+} in solutions resulting from the enhanced

https://doi.org/10.1021/jacs.5c05005
J. Am. Chem. Soc. XXXX, XXX, XXX−XXX

reaction rate at a high temperature. Careful imaging analysis of different regions in Figure 4a−e confirms that the reduced growth rate is due to the depletion of Cu^{2+} rather than an underestimation of the deposited area caused by dendritic growth outside of the field of view (Figure S12). During the later stage of growth (6−12 s), most of the Cu domains tend to grow thicker regardless of their morphologies rather than follow sharp dendrite growth in lateral directions. This behavior is likely due to the predominance of surface Cu diffusion over Cu deposition at elevated temperatures, resulting from the reduced concentration of Cu^{2+} in solution, which facilitates surface rearrangements that stabilize surface energy and make their structures more rounded.[66−68]

At 20 °C, Cu exhibits mossy growth with a relatively uniform growth front throughout the observation (Figures 4f−j, S13, S14 and Video S6). Moreover, its growth rate remained nearly constant (55.7 nm/s) during the measurement (Figure 4v). These findings indicate a uniform supply of Cu^{2+} to the growth front and balanced kinetics between the electrodeposition reaction and Cu^{2+} diffusion rates. Meanwhile, the growth rate at 80 °C is approximately 4 times higher than that at 20 °C, which demonstrates the accelerated reaction rate at elevated temperatures.[69,70] As the temperature reduced from 20 to −20 °C, Cu electrodeposition became a severely sluggish process (Figure 4k−o). As reflected by the CA current decreased from −200 nA at 20 °C to −34 nA at −20 °C (Figure S7b), the electrodeposition required prolonged reaction time to achieve a comparable level of growth. Cu electrodeposition is minimal in the first 30 s (Figure 4k,l) and achieved a mild amount of Cu dendrites from 40 to 50 s (Figure 4m,n). From 50 to 72 s, Cu dendrites abruptly started to grow on existing mossy Cu nanoislands (Figures 4n, S15, and Video S7). The Cu growth at −20 °C for 72 s is considerably slower than that at 20 °C for 20 s (Figure 4j,o). The growth behavior at −20 °C exhibits an initial growth of mossy Cu at a slow rate of 3.2 nm/s, followed by an abrupt increase to 44.3 nm/s by about 14 times with a concurrent formation of dendrites (Figures 4w and S16). The slow initial growth rate indicates a suppression of the reaction rate at a lower temperature.[70] Concurrently, the low temperature slows down Cu^{2+} diffusion to surfaces. Continuous consumption and insufficient mass transport of Cu^{2+} gradually deplete Cu^{2+} on the electrode surface.[71,72] With limited Cu^{2+} concentration at the surface, Cu deposition preferentially occurs on surface protrusions exhibiting enhanced local electric fields, thereby promoting the formation of copper dendrites.[73] The Cu dendrites formed at −20 °C feature nanometer-scale thin filament structures that preserve their sharpness over time (Figure 4n,o), which is different from μm-sized rounded Cu dendrites at 80 °C (Figure 4d,e). Such a difference is attributed to the low surface diffusion rates due to the reduced temperature, which hinders surface reconstructions into rounded structures.[67,68] The quantification of diffusion rates at various temperatures requires comprehensive electrochemical measurements in both EC-STEM and benchtop experiments and will be included in our future study.

As the temperature decreased to a very low level of −40 °C, the Cu electrodeposition ceased to happen at −2 V. A tremendous overpotential at CA of −5 V was required to initiate the Cu electrodeposition in cold liquids (Figures 4p−t, S17, Video S8). A mild growth of Cu nanoislands was observed from 0 to 20 s (Figure 4p−r) with a progressive growth of Cu nanoislands from 20 to 72 s (Figures 4r−t and S18). In line with the EC-STEM observation, the initial growth rate at −40 °C is 5.9 nm/s, which is comparable to the value of 3.2 nm/s at −20 °C (Figure 4x). Subsequently, the growth rate gradually decreases to a very slow rate of 0.7 nm/s. This comparison indicates that Cu electrodeposition kinetics at −40 °C is significantly suppressed despite the use of an exceptional overpotential of −5 V, when compared to that under a CA of −2 V at −20 °C. To investigate the reversibility of Cu electrodeposition/stripping processes, a CA of +2 V at 20 °C could completely strip away the Cu nanoislands in the organic solution within 25 s (Figure S19). In comparison, a CA of +5 V at −40 °C was not able to completely remove electrodeposited Cu after 72 s (Figure S20 and Video S9), leaving some remaining Cu nanoislands/dendrites, which resembles the dead lithium dendrite during lithium deposition/stripping studies in lithium metal battery anode.[25,26,74]

In addition to the above 1D information on quantifying the overall growth rate as a function of temperature (Figures 4u−x), we developed automated algorithms to construct violin plots for analyzing the heterogeneous 2D distribution of local growth rates and visualization of the nonuniform growth front (Figures 4y and S9, S14, S16, S18). Note that the deposition rate here is the growth rate at the growth front by quantifying image intensity normalized to the image width and time (I/(nm·s)), which is different from the above normalized 1D growth rate (nm/s). Overall, the violin plots show that both the overall and local growth slow down significantly as temperatures decrease. The maximum values of the mean growth rates decrease from ∼20 I/(nm·s) at 80 °C to ∼4 I/(nm·s) at 20 °C and a very low level of ∼0.1 I/(nm·s) at −20 and −40 °C (Figure 4y). The violin plot at 80 °C exhibits a highly nonuniform 2D distribution of growth rates with the mean value achieving a maximum level at 3 s, followed by a progressive decay until 12 s. It is consistent with the EC-STEM movies showing preferential growth events only occurring at particular nucleation sites (Figure 4a−e). In comparison, the violin plot at 20 °C exhibits more uniform growth, which matches well with the growth pattern of mossy Cu domains (Figure 4f−j,y). The drastic difference between 80 and 20 °C can be rationalized as follows: Cu electrodeposition at 80 °C has a lower energy barrier at elevated temperatures and thus a smaller overpotential than that at 20 °C (see the Arrhenius analysis in Figure S32). Under the same applied potential of −2 V, the net driving force after overcoming overpotentials is much larger at 80 °C, leading to rapid dendritic growth, relative to mossy Cu growth at 20 °C, which matches the 1D growth rate analysis well (Figure 4u,v).

While the overall temperature-dependent growth rate is well within expectation, it is worthwhile noting that the violin plot at −20 °C correctly identified a large deviation in the 2D distribution of growth rates at 50 s, which has a growth rate 3 times higher than the baseline at other time periods and corresponds to the abrupt formation of Cu dendrites starting at 50 s (Figure 4n). The contour plots of individual EC-STEM image frames reveal that growth occurs primarily at the furthest tips of Cu mossy or dendritic structures, irrespective of temperatures. In addition, the level of nonuniformity in the growth rate can be reflected in the variations of false color maps of the growth front in the contour plots (Figures S9, S14, S16, and S18, blue/red color bars). The false color variations at the growth front noticeably decay from 80 to −40 °C, suggesting that the increasing uniformity of growth rates is due to more sluggish electrodeposition kinetics at lower temperatures. In summary, the violin plot analysis effectively visualizes temperature effects on 2D nonuniform distribution of growth rates and

https://doi.org/10.1021/jacs.5c05005
J. Am. Chem. Soc. XXXX, XXX, XXX−XXX

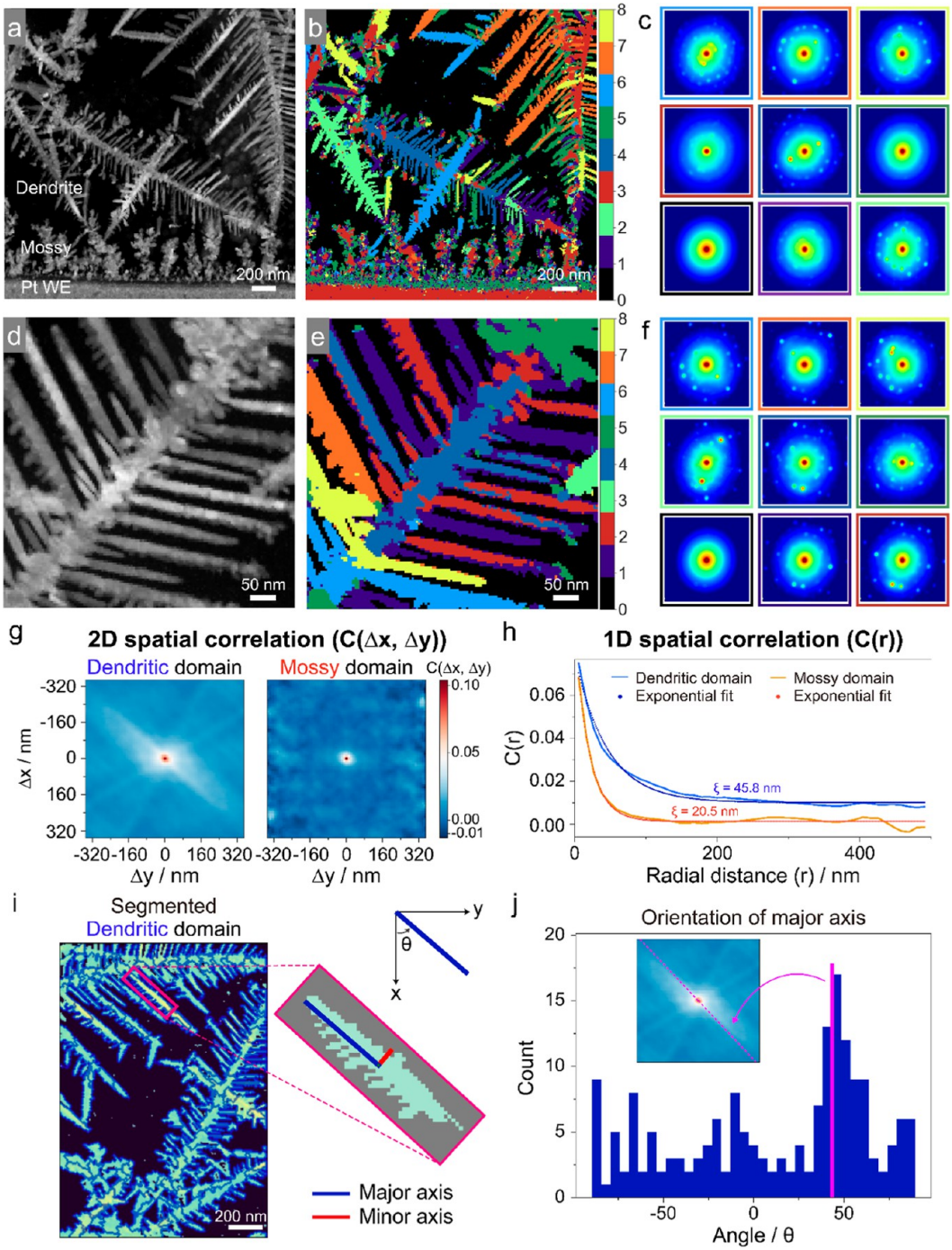

Figure 5. *Operando* 4D-STEM of Cu dendrites at −40 °C in the organic solution. (a,d) Virtual ADF-STEM image of Cu dendrites grown on the top of mossy Cu and a representative Cu dendrite. (b,c,e,f) False-color 4D-STEM clustering maps of dendritic and mossy Cu structures and corresponding electron diffraction patterns in various colors showing different crystal orientations. (g) 2D spatial correlation functions of Cu nanograins in dendritic (left) and mossy domains (right). (h) 1D spatial correlation functions and their exponential fits in dendritic and mossy domains. (i) Segmentation of dendrites and their ellipse fits for extracting orientation of their major axis. (j) A histogram for orientations of the major axis from the ellipse fit of segmented dendrites.

highlights the heterogeneity in local electrical fields governing both global growth rates and local unexpected growth due to abrupt nucleation/growth of Cu dendrites.

The quantitative analysis for the nucleation process reveals that an elevated temperature leads to a fewer number of nuclei with increased sizes (Figure 3). Furthermore, temperatures have a strong impact on the growth rates and modulate the two-step growth modes of mossy and dendritic growth (Figure 4). Elevated temperatures increase the local nonuniformity of growth rates and amplify the effects of heterogeneous local electrical fields. In principle, the different growth modes of Cu have an impact on its resulting crystal structures. Although diffusion-controlled growth leads to both mossy and dendritic Cu formation, mossy Cu develops from numerous nucleation sites, while dendritic Cu grows onto fewer protrusions.[55] In light of these distinct growth mechanisms, *operando* EC-STEM

https://doi.org/10.1021/jacs.5c05005
J. Am. Chem. Soc. XXXX, XXX, XXX−XXX

images reveal that mossy Cu features polycrystalline structures with smaller grains, while dendritic Cu forms elongated crystalline structures with larger grain sizes. Those findings demonstrate the robustness and applicability of our *operando* heating and cooling EC-STEM methods with machine learning-assisted high-throughput quantitative analysis.

Moving beyond conventional STEM imaging of morphological changes, four-dimensional (4D) STEM has the potential to retrieve structural information on complex polycrystalline structures in liquid under electrochemical conditions, which are required by most of air-sensitive energy materials. Given nanoscale Cu is subjected to rapid air exposure and forms a surface oxide layer,[36] *operando* 4D-STEM is required to study the newly formed metallic Cu dendrites, which are not accessible by conventional *ex situ* TEM studies of post-mortem samples. 4D-STEM records a full 2D reciprocal-space diffraction pattern from each point as the STEM probe is scanned over the sample and forms a 2D real-space image. 4D-STEM, based on the electron microscope pixel array detector (EMPAD), achieves single-electron sensitivity and rapid acquisition. 4D-STEM is indispensable to resolve the complex structure of beam-sensitive materials in liquids with low-dose electron diffraction.[36,75] Our previous work suggests that a thin-liquid layer is necessary to enable *operando* 4D-STEM diffraction imaging since the liquid layer in an as-assembled EC-STEM liquid cell is too thick.[75] Here, under a CA of −2 V at −20 °C for a sufficiently long time (∼600 s) (Figure S21), hydrogen bubbles were electrogenerated and repelled most of the thick liquid, leading to a thin liquid layer with significantly improved spatial resolution. Low-loss electron energy-loss spectroscopy (EELS)[76] quantified that the thin liquid layer has a liquid thickness of around 120 nm and the hydrogen bubble repelled a liquid layer of 500 nm or thicker (Figures S22 and Table S4). Given the kinetics is very sluggish to generate hydrogen bubbles in liquids at −40 °C, Cu dendrites were formed in a thin liquid at −20 °C and further cooled to −40 °C to evaluate *operando* heating/cooling EC-STEM in very cold liquids.

We performed *operando* 4D-STEM diffraction imaging in liquids at −40 °C for extended periods of time (∼1 h) to simulate battery operation in cold liquids (see animation of *operando* 4D-STEM of Cu dendrites in the liquid in Video S10).[77,78] *Operando* 4D-STEM data was acquired at a low dose of ∼ 40 e^-/Å and beam effects were routinely examined to ensure no beam damage after 4D-STEM measurements (Figure S23). *Operando* EC-STEM images reveal the growth of nanoscale mossy Cu nanoislands on the Pt WE, followed by the substantial growth of μm-sized Cu dendrites (Figure 5a). The Cu dendrites were visualized with a fishbone-shaped morphology.

A K means-based hierarchical clustering method was developed as an unsupervised machine learning method to segment gigabyte-level 4D-STEM datasets into different clusters.[79−81] While traditional STEM images show morphological changes (Figure 5a,d), 4D-STEM clustering reveals in-depth structural information on polycrystalline Cu dendrites in liquids at −40 °C (Figure 5b,c,e,f). A false-color 4D-STEM map presents a collection of Cu dendrites with various crystal orientations (Figure 5b,e). The electron diffraction pattern in black with an index of 0 represents the amorphous SiN_x/liquid background, while the electron diffraction patterns in colors with indices from 1 to 8 correspond to Cu dendrites with different crystal orientations (Figure 5c,f). Cu dendrites in Figure 5b with the same or similar colors suggest those Cu dendrites have the same or similar crystal orientations. The false-color 4D-STEM map in Figure 5b clearly presents the heterogeneous growth of Cu dendrites with dramatically different crystal orientations among different dendrites as well as different branches of the same Cu dendrite. In particular, the initially grown mossy Cu nanoislands on the Pt WE are granular with fine grain sizes of about 4800 ± 1500 nm^2 with random crystal orientations (Figure S24). In comparison, Cu dendrites grown at a later stage have five-times larger grain sizes of around 28,700 ± 3000 nm^2 with strongly preferential crystal orientations (Figure S24). The larger grain size of Cu dendrites is consistent with the faster growth rate of Cu dendrites, relative to mossy Cu domains (Figure 4w), and is likely due to strong local electrical fields at nucleation sites.[82] Figure 5e presents a magnified false-color 4D-STEM map of one individual Cu dendrite with the same color assignment of 9 different clusters. The majority of branches attached to the backbone have one dominant color, indicating one preferential crystal orientation of the individual branches. *Operando* 4D-STEM mapping of Cu dendrites in other regions supports the heterogeneous nature of Cu dendrites and mossy Cu nanoislands electrodeposited on the Pt WE in cold liquids under electrochemical conditions (Figures S25 and S26).

In addition to quantification of their grain sizes, 4D-STEM diffraction imaging datasets were quantified by correlation analysis to evaluate spatial similarities of heterogeneous crystal structures.[83] The 4D-STEM image in Figure 5a was divided into dendritic and mossy domains (Figure S27), then 2D spatial correlations of pixelated diffraction patterns were calculated in each domain, offering spatial distributions of similar diffraction patterns (Figure 5g). The 2D correlation map in the dendritic domain exhibits a strong correlation along the bright diagonal line from the upper left to the lower right, while the mossy domain map shows an irregular and darker contrast, which indicates that Cu nanograins in dendritic domains exhibit anisotropically stronger and longer structural correlations (Figure 5g). Radial integration of the 2D maps yielded 1D correlation functions that feature exponential decay, enabling the quantification of correlation length (ξ) through numerical fitting (Figure 5h). The correlation length of the dendritic domain is 45.8 ± 2.0 nm, while that of the mossy domain is more than 2 times shorter at 20.5 ± 0.9 nm, which evidence stronger spatial similarities of crystal structures in dendritic domains (Figure 5h). To elucidate the strong anisotropic signals in the 2D map of dendritic domains, the 4D-STEM image of one domain was segmented and fitted to ellipses, which yields the orientation of the major axis of segmented dendrites (Figure 5i). A histogram of the orientation shows that the most frequent orientation aligns with the angle of strong signals (43°) in the 2D correlation map, which reveals that the strong anisotropic correlation is attributed to the preferred directional growth of Cu dendrites (Figure 5j). Other strong directional correlations are also caused by the directional growth dendrites (Figure S28).

In summary, *operando* heating/cooling EC-STEM imaging, equipped with ML-assisted 4D-STEM structural mapping, reveals the temperature-, potential-, and electrolyte-dependent reaction kinetics of Cu electrodeposition and stripping processes from −40 to 95 °C. *Operando* electrochemical 4D-STEM reveals a distinct two-stage growth of granular mossy Cu domains with random orientations, followed by larger Cu dendrites with preferred directional growth. With *operando* heating/cooling EC-STEM imaging and diffraction analysis well demonstrated, electrochemistry performed in the specialized liquid cell must be

https://doi.org/10.1021/jacs.5c05005
J. Am. Chem. Soc. XXXX, XXX, XXX−XXX

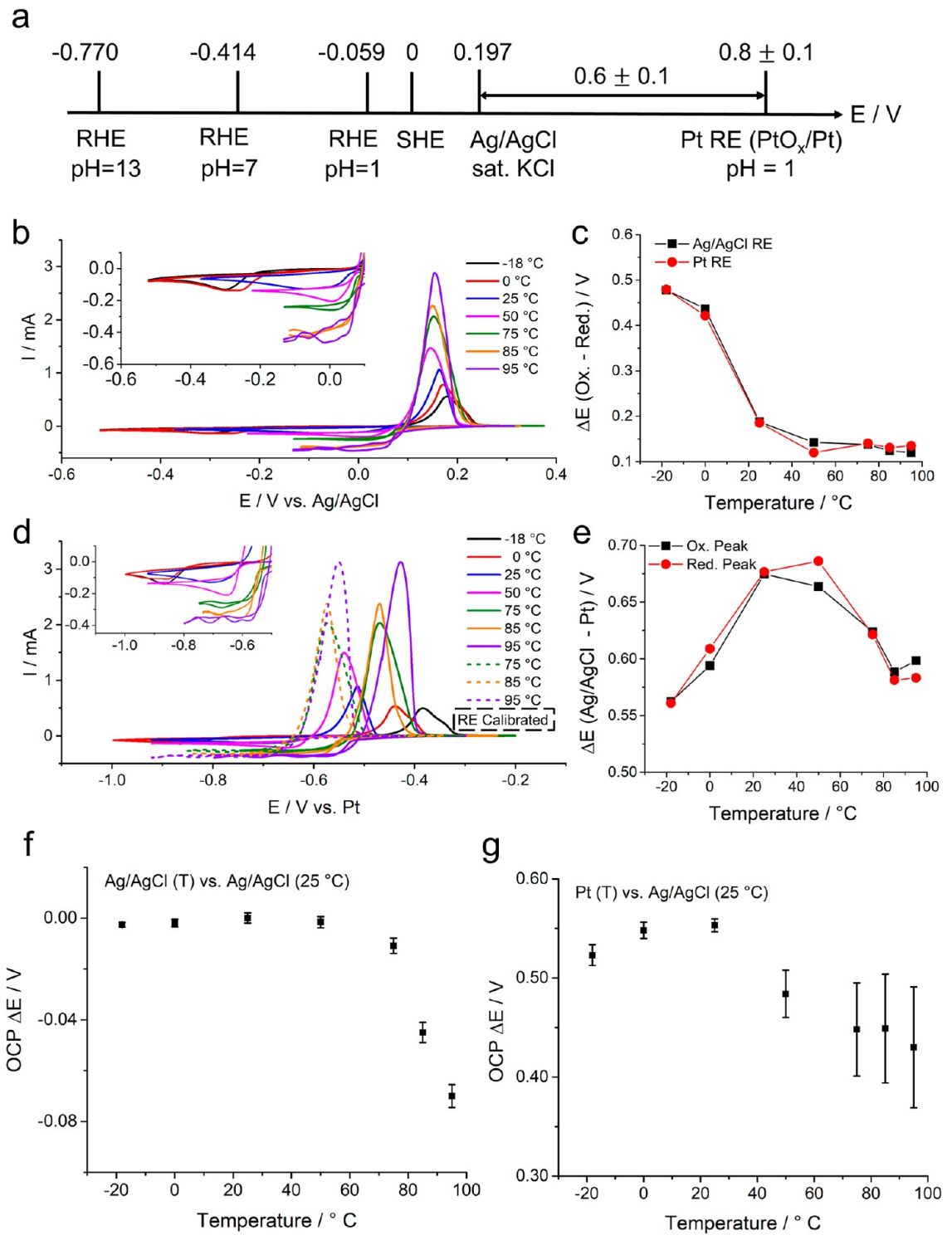

Figure 6. Benchmarking temperature-dependent electrochemistry of Cu electrodeposition/stripping in a standard three-electrode cell. (a) A summary of potential values of various reference electrodes at 25 °C. (b,d) CV profiles of Cu electrodeposition/stripping (reduction/oxidation) processes in 10 mM $CuSO_4$/0.1 M H_2SO_4 using Ag/AgCl (saturated KCl) RE (b) and Pt wire pseudo-RE (d) under various temperatures from −18 to 95 °C. Dashed lines are CV profiles at 75−95 °C after calibrating the Pt RE at given temperatures based on (g). (c) Oxidation (Ox.) and reduction (Red.) peak potential differences decrease as the temperature increases, indicating enhanced electrochemical reaction reversibility. (e) The nonmonotonic changes of potential differences between Ag/AgCl and Pt REs as the temperature increases, indicating both RE potentials are temperature dependent. (f) OCP measurements of Ag/AgCl RE under various temperatures against Ag/AgCl RE at 25 °C. Both Ag/AgCl REs are in a saturated KCl solution. (g) Pt RE under various temperatures against Ag/AgCl in saturated KCl at 25 °C.

validated by benchtop (standard) electrochemical measurements. Temperature not only impacts the reaction kinetics at the WE but also changes the RE potential, which serves as the necessary reference point for quantifying the driving force (applied potentials).

https://doi.org/10.1021/jacs.5c05005
J. Am. Chem. Soc. XXXX, XXX, XXX−XXX

Benchtop electrochemical measurements of Cu electrodeposition and stripping processes were performed in a standard three-electrode H-cell with Ag/AgCl (saturated (sat.) KCl) as the standard RE and with Pt pseudo-RE used in this EC-STEM work, as well as other *in situ* electrochemical liquid-cell TEM studies (Figure 6). A summary of the potential conversion axis at 25 °C is presented in Figure 6a to serve as a guide for discussion here with commonly used reference electrodes. The SHE stands for the standard hydrogen electrode with its value defined arbitrarily at 0 V under any temperature. The RHE is the reversible hydrogen electrode and is pH-dependent on the SHE scale based on the Nernst equation ($E_{RHE} = E_{SHE} - 0.0592 \cdot pH$) at 25 °C, which serves as a convenient pH-independent RE on the RHE scale for electrochemical reactions involving protons. The Ag/AgCl (saturated KCl) is a widely used commercial RE and has a potential of 0.197 V at 25 °C with a negligible potential drift of 1−2 mV over extended periods of time. The saturated KCl (~4 M KCl solution at 25 °C with excessive KCl salt) is used to prevent any positive potential drift of the RE due to gradual diffusion and dilution of KCl solution in contact with the testing electrolyte (e.g., 10 mM $CuSO_4$ + 0.1 M H_2SO_4). For instance, Ag/AgCl in 1 M KCl has a potential of 0.235 V vs SHE, 38 mV higher than that of Ag/AgCl in saturated KCl (0.197 V vs SHE) at 25 °C.[84]

The benchtop CV experiments of Cu electrodeposition and stripping were performed on Pt WE in 10 mM $CuSO_4$ and 0.1 M H_2SO_4 at 20 mV/s (Figure 6b). A standard electrochemical liquid cell with three electrodes was immersed in a temperature-controlled setup with 0 and −18 °C achieved by an ice bath and a salt bath, respectively (Figure S29). The reference electrodes used were a commercial Ag/AgCl (saturated KCl) and a Pt wire. As the temperature increased from −18 to 95 °C, the Cu stripping current increased from ~0.5 to ~3 mA with either the Ag/AgCl RE or the Pt pseudo-RE (Figure 6b,d), which qualitatively agrees with the positive current−temperature correlations with the Pt pseudo-RE in EC-STEM (Figure 2a,b). The electrodeposition/stripping (cathodic/anodic) peak potential differences decrease from 480 mV at −18 °C to 140 mV at 95 °C with both the Ag/AgCl RE and the Pt pseudo-RE, which indicates significantly improved reaction reversibility (Figure 6c). It qualitatively matches the decaying trend in the redox peak potential differences from ~220 mV at 5 °C to ~78 mV at 95 °C in the aqueous solution (Figure 2a,b). Overall, the curvatures and amplitude of CV profiles with Ag/AgCl RE are very similar to those with the Pt pseudo-RE (Figures 6b−d). The redox peak potential differences are very similar between Ag/AgCl and Pt pseudo-RE (Figure 6c). It indicates that switching from Ag/AgCl RE to Pt pseudo-RE mainly shifts the potential values of Cu electrodeposition/stripping peaks without altering the nature of redox couples. However, noticeable deviations occurred for CV profiles at 75−95 °C with the Pt pseudo-RE (green line in Figure 6d). The Cu stripping peaks at 75−95 °C are located in between stripping peaks of 0 and 25 °C instead of on the left of stripping peaks of 50 °C as anticipated by the left-shift trend from −18 to 50 °C and higher temperatures. CV profiles vs Pt pseudo-RE at 75−95 °C, with similar corrections (Figure 6d, dashed profiles), are very similar to CV profiles vs Ag/AgCl at 75−95 °C (Figure 6b) and indicate the potential corrections are effective in addressing the shift of Pt pseudo-RE at elevated temperatures.

To elucidate the origin of the deviations of CV profiles with the Pt pseudo-RE at 75−95 °C, Cu stripping (oxidation, ox.) and electrodeposition (reduction, red.) peak potentials were used as metrics to calculate the potential differences between Ag/AgCl RE and Pt pseudo-RE (Figure 6e). The ox. or red. peak potential differences show a progressive increase from 0.55 to 0.67 V from −18 to 20 °C, followed by a sharp decay to ~0.60 V as the temperature further increased to 95 °C. Overall, the potential difference between Ag/AgCl RE and Pt pseudo-RE is around 0.60 V. The nonmonotonic changes of potential differences between two REs indicate that the potentials of both Ag/AgCl RE and Pt pseudo-RE are temperature-dependent. Thus, careful temperature calibration of the RE is necessary for quantifying temperature-controlled nanoscale electrochemistry. We conducted temperature calibration experiments by measuring the OCP between the two REs under controlled temperatures (T) and Ag/AgCl (sat. KCl) at a constant room temperature of 25 °C (Figures 6f,g). The Ag/AgCl RE (T) vs Ag/AgCl (25 °C) shows a minimal change (<5 mV) between −18 and 50 °C and a mild decrease by 10 and 70 mV as the temperature increased to 75 and 95 °C, respectively. It is consistent with the decaying trend of the Ag/AgCl potential at higher temperatures reported by Bard and Greeley et al.[85,86] Similarly, we calibrated the potential of the RHE at various temperatures against Ag/AgCl (25 °C) (Figure S30). It shows a near linear increase of the RHE potential between 25 and 65 °C with a mild increase of 6 mV every 10 °C. In contrast, the OCP measurements between Pt pseudo-RE at various temperatures and Ag/AgCl (25 °C) show a relatively stable value of 550 ± 10 mV between −18 and 20 °C with a significant decay to 480 ± 24 mV at 50 °C and 450 ± 50 mV at 75 °C. While the decay of Ag/AgCl RE from 25 to 75 °C is 10 mV, that of Pt pseudo-RE under the same temperature change is ~100 mV with a large error bar of ~50 mV. Thus, the negative shift of Pt pseudo-RE at elevated temperatures is the primary reason for the noticeable decay of the peak potential differences from 25 to 95 °C in Figure 6e. In other words, the whole CV profiles at 75, 85, and 95 °C were shifted negatively due to the temperature-induced negative shift of the Pt pseudo-RE (Figure 6d). A ca. 100 mV drift correction was applied to compensate for the drift of CV profiles at 75−95 °C (Figure S31), showing the stripping peak with Pt pseudo-RE shows the correct trend, which is very similar to that with Ag/AgCl RE across the whole temperature range from −18 to 95 °C (Figure 6b). For clarity, only the temperature-corrected CV profiles at 75, 85, and 95 °C are displayed in Figures 6d and S31a. As shown in Figures 6g and S31b, the maximum possible error at uncorrected temperatures is ca. 100 mV at 75−95 °C, being much lower, ca. 20 mV, at low temperatures (0 and −18 °C), relative to 25 °C (Figure S31). In summary, the Cu electrodeposition/stripping peak potential differences show a value around 0.60 V, while the OCP measurements with the use of two REs show a value around 0.55 V with the use of Pt pseudo-RE vs Ag/AgCl. Therefore, a potential conversion of +0.6 V with a conservative uncertainty of 0.1 V between Pt pseudo-RE (pH = 1) and Ag/AgCl (sat. KCl) RE is shown in Figure 6a. The potential conversion axis points out the potential of Pt pseudo-RE (pH = 1) is 0.8 ± 0.1 V vs SHE, which is consistent with previous reports.[75,76]

Although both CV profiles obtained in benchtop experiments (Figure 6b,d) and the EC-STEM setup (Figure 2a,b) show an increasing redox current at increasing temperatures, they show a noticeable discrepancy in the amplitude of the current increase. While the benchtop experiments show a factor of 2 increase from 1 to 2 mA in the stripping current and −0.12 to −0.25 mA in the electrodeposition current from 25 to 75 °C (Figure 6b), EC-STEM shows a factor of 10 increase from 230 to 2450 nA in the

https://doi.org/10.1021/jacs.5c05005
J. Am. Chem. Soc. XXXX, XXX, XXX−XXX

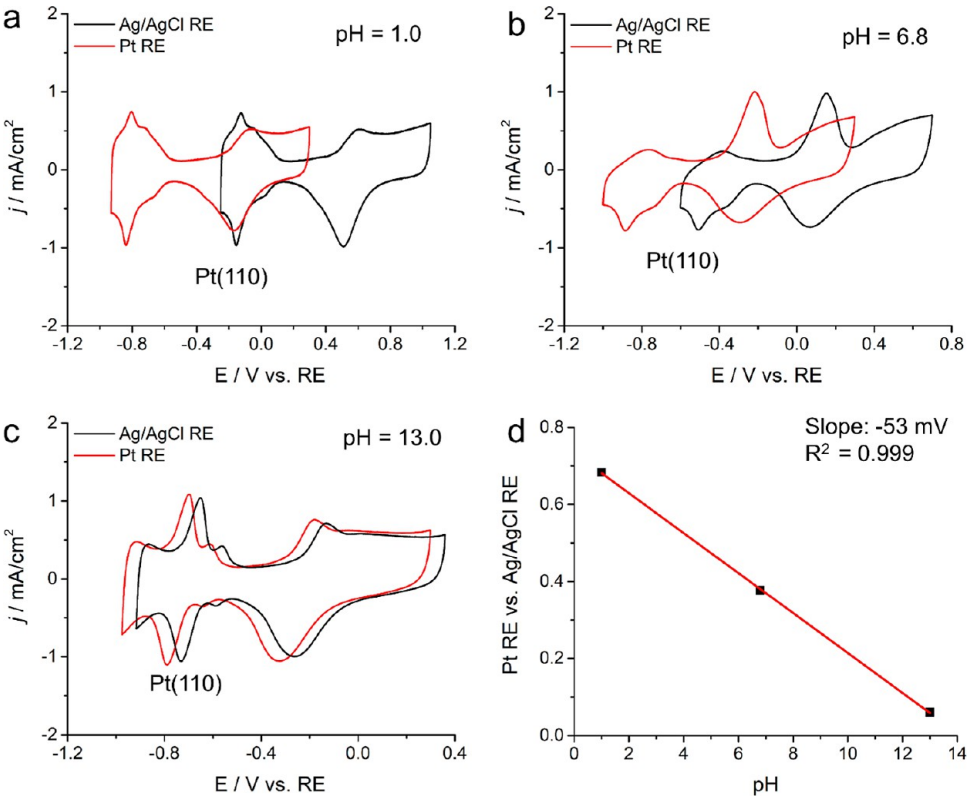

Figure 7. CV of Pt at 5 mV/s using Ag/AgCl (sat. KCl) and Pt RE in a standard three-electrode cell in solutions with a (a) pH of 1 in a strong acid (Ar-saturated 0.1 M $HClO_4$), (b) neutral pH of 6.8 in CO_2-saturated 0.1 M $KHCO_3$ (buffered solution), and (c) pH of 13 in a strong base (Ar-saturated 0.1 M KOH). (d) A summary of Pt(110) peak potential differences between Pt RE and Ag/AgCl RE with a slope of 53 ± 1 mV, which exhibits a near-Nernstian shift on the SHE scale and indicates the Pt RE potential is independent of the RHE scale.

stripping current and from −70 to −1016 nA in the electrodeposition current from 20 to 70 °C (Figure 2a). To investigate the possible kinetic and/or mass transport effects, a Tafel analysis was conducted between the Cu stripping current and overpotential (η) since the Cu stripping process is not mass transport limited by the amount of the solid Cu reactant (Figure S32). The exchange current density was extrapolated from the large overpotential region of the Tafel analysis and used for the Arrhenius plot ($\ln(I)$ vs $1/T$) to estimate the activation energy barrier (E_a). The Cu stripping process in EC-STEM exhibits an E_a value of 45.0 ± 1.2 kJ/mol, which is slightly higher but comparable to that in benchtop experiments (40.2 ± 1.2 kJ/mol). The small difference in activation energy may not fully explain the discrepancy in the amplitude of the increase in the stripping current between the EC-STEM and benchtop setup. Other factors may also play a role, including the temperature-dependent diffusion processes of Cu^{2+} and counteranions in highly confined liquid layers, as well as Cu underpotential deposition (UPD) kinetics on Pt substrates.[55]

With a thorough investigation of the temperature-dependent behavior of Pt pseudo-RE, Ag/AgCl, and RHE, the last section of this work aims to provide a rigorous analysis of pH-dependent behaviors of Pt pseudo-RE (Figure 7). We conducted pH-dependence experiments of the Pt pseudo-RE in a standard three-electrode cell (Figures S33 and 34) with a future plan to perform real-time RE calibration in EC-STEM. Figure 7a presents a well-defined CV of polycrystalline Pt nanoparticles (3 nm) deposited on the inert glassy carbon electrode in a strong acid (pH = 1) with Ar-saturated 0.1 M $HClO_4$ at 5 mV/s. The CV of Pt shows a well-resolved hydrogen region (−0.2 to 0.2 V vs Ag/AgCl) involving hydrogen underpotential deposition (UPD) and oxidation and the oxygenated species region (0.2−1.0 V vs Ag/AgCl) involving OH adsorption/desorption and Pt oxidation/reduction. The distinct H_{UPD} peak at around −0.155 V vs Ag/AgCl (~0.1 V vs RHE) is the characteristic peak of Pt(110) facets[87] and can be used as a fingerprint to track the shift of CV profiles (Figure S33). In other words, CV profiles of Pt can be used to calibrate the potential of Pt RE against the Ag/AgCl RE at various pH values. When the Ag/AgCl RE was switched to Pt pseudo-RE, the whole CV profile shifted negatively with Pt(110) located at −0.837 V vs Pt RE. Those two independent measurements suggest the potential of Pt RE is 0.693 V vs Ag/AgCl (Figure S34). CV profiles of Pt were then performed at a neutral pH value of 6.8 with buffered solution (CO_2-saturated 0.1 M $KHCO_3$), which is commonly used for evaluating the performance of CO_2 reduction electrocatalysts (Figure 7b). CV peaks of Pt(110) remain distinguishable and are used to calculate the potential of Pt RE as 0.377 V vs Ag/AgCl (Figure S35). In a strong base (Ar-saturated 0.1 M KOH), the Pt(110) peak potential differences are even smaller, leading to the potential of Pt RE being 0.060 V vs Ag/AgCl (Figure S36). Given the positions of Pt(110) peaks with Pt pseudo-RE experience a significant positive shift as the pH increases from 1 to 13, the Pt(110) peak potential differences with the use of Pt RE and the Ag/AgCl RE are plotted in Figure 7d. A strong linear correlation with a R^2 of 0.999 shows a slope of −53 mV. It is close to the ideal Nernstian shift of −59 mV for the pH-dependent behavior of Pt pseudo-RE, pointing out an important implication: Pt pseudo-RE with a native Pt oxide layer is pH-dependent on the SHE scale but pH-independent of the RHE

https://doi.org/10.1021/jacs.5c05005
J. Am. Chem. Soc. XXXX, XXX, XXX−XXX

scale. A generalized half equation of Pt pseudo-RE can be expressed in eq 1.

$$PtO_x + 2xe^- + 2xH^+ \rightleftharpoons Pt + xH_2O \quad (1)$$

The Pt pseudo-RE with a PtO_x/Pt redox couple shows a near-Nernstian pH dependence and can serve as a convenient pH-independent RE on the RHE scale in strong acid, strong base, or buffered solutions. In an unbuffered solution (bulk pH = 7, Ar-saturated 0.1 M $NaClO_4$), the Pt(110) peak differences between Pt pseudo-RE and Ag/AgCl RE result in a value of 0.517 V, which deviates from the value (0.377 V) obtained in buffered solution (Figure S37). It indicates a surface pH of around 4 based on the linear correlation, suggesting a noticeable deviation of the surface pH from the bulk pH of 7. CV of Pt nanoparticles with Pt pseudo-RE in a three-electrode cell, with a porous glass frit separating the WE from the RE, suggests that Pt pseudo-RE delivers remarkable stability with the drift of the RE less than 5 mV during 2 h extended periods of CV tests (Figure S38). In typical CV experiments with Pt pseudo-RE in the EC-STEM setup, the Pt(110) peak shows a potential of -0.7 ± 0.1 V vs Pt (Figure S39). The large uncertainty comes from the inherent lack of a salt bridge to block the interference of the PtO_x/Pt RE by the nearby WE and CE (Figure 1e). Given Pt(110) is around 0.1 V vs SHE, the potential of Pt pseudo-RE (pH = 1) is 0.8 ± 0.1 V vs SHE in the EC-STEM setup. This potential conversion of 0.8 V (PtO_x/Pt (pH = 1) vs SHE), based on the CV of Pt, has an excellent agreement with the early potential conversion of 0.6 V (PtO_x/Pt (pH = 1) vs Ag/AgCl), based on the CV of Cu electrodeposition/stripping processes (Figure 6a). In summary, systematic electrochemical measurements of Cu electrodeposition/stripping processes and Pt examine the temperature-dependent and pH-dependent behaviors of Pt pseudo-RE (PtO_x/Pt) used in the EC-STEM setup and calibrate the RE values against Ag/AgCl. At pH = 1, the potential of Pt pseudo-RE is $+0.6 \pm 0.1$ V vs Ag/AgCl and $+0.8 \pm 0.1$ V vs SHE. Across a wide range of pH values, the potential of Pt pseudo-RE follows a near-Nernstian pH-dependent behavior on the SHE scale, indicating the robustness of the Pt pseudo-RE in strong acid or base conditions for fuel cell or water electrolyzer applications or neutral buffered solution for the CO_2 reduction reaction.

CONCLUSION

In conclusion, we have demonstrated *operando* heating and cooling EC-STEM with electrochemical and thermal control with access to a wide temperature range of −50 to 300 °C. Such an *operando* method has been employed to investigate Cu electrodeposition and deposition processes at nanoscale solid−liquid interfaces from −40 to 95 °C. *Operando* heating−cooling EC-STEM reveals strong temperature- and potential-dependent heterogeneous growth of Cu nanostructures in both aqueous and organic solutions. *Operando* electrochemical 4D-STEM, assisted by machine learning, reveals the initial growth of granular Cu nanoislands, followed by micrometer-large Cu dendrites in cold liquids. Close examination of the temperature dependence of the Pt pseudo-RE and Ag/AgCl RE reveals that the Pt RE experiences a significant negative potential shift at elevated temperatures, while the Ag/AgCl RE remains relatively stable. The pH-dependent studies of the Pt RE point out the reliability of the Pt RE across a wide pH range from 1 to 13. The 0.1 V uncertainty of the Pt pseudo-RE is not a severe issue in electrochemical reactions requiring large overpotentials, such as the CO_2 reduction reaction and oxygen reduction/evolution reactions. However, other electrochemical reactions with small overpotentials, such as hydrogen oxidation/evolution reactions, demand a higher accuracy of the RE. Future *operando* heating/cooling EC-STEM studies on temperature effects on electrochemical kinetics, mass transport, and beam-induced radiolysis[88−90] will increase the robustness of this rapidly developing method. We anticipate that *operando* electrochemical 4D-STEM with a higher temporal resolution will become feasible to track rapid structural evolution given the continuous development of faster and more sensitive 4D-STEM electron detectors.[91] With continuous advances in techniques, we foresee that *operando* heating/cooling EC-STEM, equipped with ML-assisted 4D-STEM, will revolutionize our mechanistic understanding of nanoscale electrochemical dynamics of energy materials under realistic climates. *Operando* methods developed here will help us understand catalyst activation or degradation mechanisms under elevated temperatures and battery fatigue under varying temperatures or failure mechanisms under extremely cold or hot climates. These findings open the door for investigating temperature-controlled nanoscale electrochemistry as an emerging new branch of modern electrochemistry, in particular, and physical chemistry in general.

ASSOCIATED CONTENT

Supporting Information

The Supporting Information is available free of charge at https://pubs.acs.org/doi/10.1021/jacs.5c05005.

Experimental section; EC- and 4D-STEM imaging analysis; temperature calibration and EELS liquid thickness quantification; captions including descriptions of EC-STEM movies and setup schematics; supporting references; and additional experimental details, materials, and methods, including photographs of the experimental setup (PDF)

Descriptions of EC-STEM movies and setup schematics (ZIP)

AUTHOR INFORMATION

Corresponding Author

Yao Yang − *Department of Chemistry and Chemical Biology, Baker Lab, Cornell University, Ithaca, New York 14853, United States; Kavli Institute at Cornell for Nanoscale Science, Cornell University, Ithaca, New York 14853, United States;* orcid.org/0000-0003-0321-3792; Email: yaoyang@cornell.edu

Authors

Sungin Kim − *Department of Chemistry and Chemical Biology, Baker Lab, Cornell University, Ithaca, New York 14853, United States;* orcid.org/0000-0001-9107-0781

Valentin Briega-Martos − *Department of Chemistry and Chemical Biology, Baker Lab, Cornell University, Ithaca, New York 14853, United States;* orcid.org/0000-0001-8407-2260

Shikai Liu − *Department of Chemistry and Chemical Biology, Baker Lab, Cornell University, Ithaca, New York 14853, United States*

Kwanghwi Je − *Department of Chemistry and Chemical Biology, Baker Lab, Cornell University, Ithaca, New York 14853, United States*

https://doi.org/10.1021/jacs.5c05005
J. Am. Chem. Soc. XXXX, XXX, XXX−XXX

Chuqiao Shi − *Department of Materials Science and Nano Engineering, Rice University, Houston, Texas 77005, United States*
Katherine Marusak Stephens − *Protochips Inc., Morrisville, North Carolina 27560, United States*
Steven E. Zeltmann − *Platform for the Accelerated Realization, Analysis, and Discovery of Interface Materials, Cornell University, Ithaca, New York 14853, United States*
Zhijing Zhang − *Department of Chemistry and Chemical Biology, Baker Lab, Cornell University, Ithaca, New York 14853, United States*
Rafael Guzman-Soriano − *Department of Chemistry and Chemical Biology, Baker Lab, Cornell University, Ithaca, New York 14853, United States*
Wenqi Li − *Department of Chemistry and Chemical Biology, Baker Lab, Cornell University, Ithaca, New York 14853, United States*
Jiahong Jiang − *Department of Chemistry and Chemical Biology, Baker Lab, Cornell University, Ithaca, New York 14853, United States;* orcid.org/0009-0004-8750-2560
Juhyung Choi − *Department of Chemistry and Chemical Biology, Baker Lab, Cornell University, Ithaca, New York 14853, United States;* orcid.org/0000-0003-0770-6113
Yafet J. Negash − *Department of Chemistry and Chemical Biology, Baker Lab, Cornell University, Ithaca, New York 14853, United States*
Franklin S. Walden, II − *Protochips Inc., Morrisville, North Carolina 27560, United States*
Nelson L. Marthe, Jr. − *Protochips Inc., Morrisville, North Carolina 27560, United States*
Patrick S. Wellborn − *Protochips Inc., Morrisville, North Carolina 27560, United States*
Yaofeng Guo − *Protochips Inc., Morrisville, North Carolina 27560, United States*
John Damiano − *Protochips Inc., Morrisville, North Carolina 27560, United States*
Yimo Han − *Department of Materials Science and Nano Engineering, Rice University, Houston, Texas 77005, United States;* orcid.org/0000-0003-0563-4611
Erik H. Thiede − *Department of Chemistry and Chemical Biology, Baker Lab, Cornell University, Ithaca, New York 14853, United States*

Complete contact information is available at: https://pubs.acs.org/10.1021/jacs.5c05005

Author Contributions

#S.K. and V.B.M. contributed equally.

Notes

The authors declare no competing financial interest.

■ ACKNOWLEDGMENTS

This work was supported by the Center for Alkaline-Based Energy Solutions (CABES), an Energy Frontier Research Center (EFRC) program supported by the U.S. Department of Energy, under grant DE-SC0019445. This work was supported by the Cornell Atkinson Center for Sustainability and the 2030 Project: A Cornell Climate Initiative. We acknowledge the generous support from the Kavli Institute at Cornell (KIC) Instrumentation Grant. This work made use of TEM facilities at the Cornell Center for Materials Research (CCMR), which are supported through the National Science Foundation Materials Research Science and Engineering Center (NSF MRSEC) program (DMR-1719875). Y.H. acknowledges NSF (CMMI-2239545), Welch Foundation (C-2065), and American Chemical Society Petroleum Research Fund (67236-DNI10). This work was performed in part at the Analytical Instrumentation Facility (AIF) at North Carolina State University, which is supported by the State of North Carolina and the National Science Foundation (award number ECCS-2025064). The AIF is a member of the North Carolina Research Triangle Nanotechnology Network (RTNN), a site in the National Nanotechnology Coordinated Infrastructure (NNCI). We appreciate the dedicated support from John Grazul and Philip Carubia in maintaining the Perseus STEM for *operando* EC-STEM experiments at CCMR. S.K. and J.C. are supported by the National Research Foundation of Korea (NRF) grant funded by the Korea government (MSIT) (RS-2024-00351910 and RS-2024-00414454, respectively). K.J. is supported by the Eric and Wendy Schmidt AI in Science Postdoctoral Fellowship, a program of Schmidt Sciences, LLC. S.E.Z. acknowledges support from the Platform for the Accelerated Realization, Analysis, and Discovery of Interface Materials (PARADIM), by the National Science Foundation under Cooperative Agreement No. DMR-2039380. We acknowledge the help on schematic design from Madeline DeGroodt, Jennifer McConnell, and Zayna King.

■ REFERENCES

(1) Avery, H. E. *Basic Reaction Kinetics and Mechanisms*; Springer: New York, 1974; p 47.
(2) Gibert, T. R.; Kirss, R. V.; Foster, N.; Davies, G. *Chemistry: The Science in Context*, 4th ed., W. W. Norton & Company: New York, 2014; p 694.
(3) Li, J.; Kuang, Y.; Zhang, X.; Hung, W.; Chiang, C.; Zhu, G.; Chen, G.; Wang, F.; Liang, P.; Dai, H. Electrochemical acetate production from high-pressure gaseous and liquid CO_2. *Nat. Catal.* **2023**, *6*, 1151−1163.
(4) Jacobs, T. S.; Park, S.; Schönig, M.; Weckhuysen, B. M.; Koper, M. T. M.; van der Stam, W. Luminescence thermometry probes local heat effects at the platinum electrode surface during alkaline water electrolysis. *ACS Energy Lett.* **2024**, *9*, 3335−3341.
(5) Ryu, J.; Bregante, D. T.; Howland, W. C.; Bisbey, R. P.; Kaminsky, C. J.; Surendranath, Y. Thermochemical aerobic oxidation catalysis in water can be analysed as two coupled electrochemical half-reactions. *Nat. Catal.* **2021**, *4*, 742−752.
(6) Shen, K.; Wang, Z.; Bi, X.; Ying, Y.; Zhang, D.; Jin, C.; Hou, G.; Cao, H.; Wu, L.; Zheng, G.; Tang, Y.; Tao, X.; Lu, J. Magnetic Field-Suppressed Lithium Dendrite Growth for Stable Lithium-Metal Batteries. *Adv. Energy Mater.* **2019**, *9*, 1900260.
(7) Curcio, A.; Wang, J.; Wang, Z.; Zhang, Z.; Belotti, A.; Pepe, S.; Effat, M. B.; Shao, Z.; Lim, J.; Ciucci, F. Unlocking the Potential of Mechanochemical Coupling: Boosting the Oxygen Evolution Reaction by Mating Proton Acceptors with Electron Donors. *Adv. Funct. Mater.* **2021**, *31*, 2008077.
(8) Patterson, J. E.; Hunsaker, H. N.; Smith, L. C.; Sansom, R. L.; Asplund, M. C. Modified Iodine Clock Reaction to Introduce the Concept of Activity. *J. Chem. Educ.* **2024**, *101*, 4051−4056.
(9) Laidler, K. The Development of the Arrhenius Equation. *J. Chem. Educ.* **1984**, *61*, 494−498.
(10) Atkins, P.; de Paula, J.; Keeler, J. *Atkin's Physical Chemistry*, 8th ed., W. H. Freeman and Company, New York, 2002; p 560.
(11) Xia, Y.; Xia, X.; Peng, H.-C. Shape-Controlled Synthesis of Colloidal Metal Nanocrystals: Thermodynamic versus Kinetic Products. *J. Am. Chem. Soc.* **2015**, *137*, 7947−7966.
(12) Appl, M. *The Haber−Bosch Process and the Development of Chemical Engineering*, A Century of Chemical Engineering; Plenum Press: New York, 1982; pp 29−54.

(13) Akers, W. W.; Camp, D. P. Kinetics of the Methane-Steam Reaction. *AIChE J.* **1955**, *1*, 471−475.
(14) Dry, M. E. The Fischer−Tropsch process: 1950−2000. *Catal. Today* **2002**, *71*, 227−241.
(15) Lee, S.; Fleuren, N. F. J.; Pinkowitz, A.; Ross, F. M. Patterned Electrochemical Deposition through Local Heating of Electrodes. *J. Electrochem. Soc.* **2025**, *172*, 022506.
(16) Yang, Y.; et al. Electrocatalysis in Alkaline Media and Alkaline Membrane-Based Energy Technologies. *Chem. Rev.* **2022**, *122*, 6117−6321.
(17) Xiong, Y.; Yang, Y.; Joress, H.; Padgett, E.; Gupta, U.; Yarlagadda, V.; Agyeman-Budu, D. N.; Huang, X.; Moylan, T. E.; Zeng, R.; Kongkanand, A.; Escobedo, F. A.; Brock, J. D.; DiSalvo, F. J.; Muller, D. A.; Abruña, H. D. Revealing the Atomic Ordering of Binary Intermetallics Using In Situ Heating Techniques at Multilength Scales. *Proc. Natl. Acad. Sci. U.S.A.* **2019**, *116*, 1974−1983.
(18) Li, Q.; Molina Villarino, A.; Peltier, C. R.; Macbeth, A. J.; Yang, Y.; Kim, M.; Shi, Z.; Krumov, M. R.; Lei, C.; Rodríguez-Calero, G. G.; Soto, J.; Yu, S.; Mutolo, P. F.; Xiao, L.; Zhuang, L.; Muller, D. A.; Coates, G. W.; Zelenay, P.; Abruña, H. D. Anion Exchange Membrane Water Electrolysis: The Future of Green Hydrogen. *J. Phys. Chem. C* **2023**, *127*, 7901−7912.
(19) Pivovar, B. Catalysts for Fuel Cell Transportation and Hydrogen Related Uses. *Nat. Catal.* **2019**, *2*, 562−565.
(20) Meier, J. C.; Galeano, C.; Katsounaros, I.; Witte, J.; Bongard, H. J.; Topalov, A. A.; Baldizzone, C.; Mezzavilla, S.; Schüth, F.; Mayrhofer, K. J. J. Design Criteria for Stable Pt/C Fuel Cell Catalysts. *Beilstein J. Nanotechnol.* **2014**, *5*, 44−67.
(21) Liu, Y.; Zhu, Y.; Cui, Y. Challenges and Opportunities towards Fast-Charging Battery Materials. *Nat. Energy* **2019**, *4*, 540−550.
(22) Jaguemont, J.; Boulon, L.; Dubé, Y. A Comprehensive Review of Lithium-Ion Batteries Used in Hybrid and Electric Vehicles at Cold Temperatures. *Appl. Energy* **2016**, *164*, 99−114.
(23) Ratnakumar, B. V.; Smart, M. C.; Huang, C. K.; Perrone, D.; Surampudi, S.; Greenbaum, S. G. Lithium Ion Batteries for Mars Exploration Missions. *Electrochim. Acta* **2000**, *45*, 1513−1517.
(24) Yuksel, T.; Michalek, J. Effects of Regional Temperature on Electric Vehicle Efficiency, Range, and Emissions in the United States. *Environ. Sci. Technol.* **2015**, *49*, 3974−3980.
(25) Wang, J.; et al. Improving Cyclability of Li metal Batteries at Elevated Temperatures and its Origin Revealed by Cryo-Electron Microscopy. *Nat. Energy* **2019**, *4*, 664−670.
(26) Peled, E.; Menkin, S. Review-SEI: Past, Present and Future. *J. Electrochem. Soc.* **2017**, *164*, A1703−A1719.
(27) Yang, Y.; Feijóo, J.; Briega-Martos, V.; Li, Q.; Krumov, M.; Merkens, S.; De Salvo, G.; Chuvilin, A.; Jin, J.; Huang, H.; Pollock, C. J.; Salmeron, M. B.; Wang, C.; Muller, D. A.; Abruña, H. D.; Yang, P. Operando Methods: A New Era of Electrochemistry. *Curr. Opin. Electrochem.* **2023**, *42*, 101403.
(28) Yang, Y.; Xiong, Y.; Zeng, R.; Lu, X.; Krumov, M.; Huang, X.; Xu, W.; Wang, H.; DiSalvo, F. J.; Brock, J. D.; Muller, D. A.; Abruña, H. D. Operando Methods in Electrocatalysis. *ACS Catal.* **2021**, *11*, 1136−1178.
(29) Bañares, M. A. Operando Methodology: Combination of In Situ Spectroscopy and Simultaneous Activity Measurements under Catalytic Reaction Conditions. *Catal. Today* **2005**, *100*, 71−77.
(30) Weckhuysen, B. M. Snapshots of a Working Catalyst: Possibilities and Limitations of In Situ Spectroscopy in the Field of Heterogeneous Catalysis. *Chem. Commun.* **2002**, 97−110.
(31) Williamson, M. J.; Tromp, R. M.; Vereecken, P. M.; Hull, R.; Ross, F. M. Dynamic Microscopy of Nanoscale Cluster Growth at the Solid-Liquid Interface. *Nat. Mater.* **2003**, *2*, 532−536.
(32) Serra-Maia, R.; Kumar, P.; Meng, A. C.; Foucher, A. C.; Kang, Y.; Karki, K.; Jariwala, D.; Stach, E. A. Nanoscale Chemical and Structural Analysis during In Situ Scanning/Transmission Electron Microscopy in Liquids. *ACS Nano* **2021**, *15*, 10228−10240.
(33) Kim, S.; Kwag, J.; Lee, M.; Kang, S.; Kim, D.; Oh, J.-G.; Heo, Y.-J.; Ryu, J.; Park, J. Unraveling Serial Degradation Pathways of Supported Catalysts through Reliable Electrochemical Liquid-Cell TEM Analysis. *J. Am. Chem. Soc.* **2025**, *147*, 181−191.
(34) Shen, T. H.; Spillane, L.; Peng, J.; Shao-Horn, Y.; Tileli, V. Switchable Wetting of Oxygen-Evolving Oxide Catalysts. *Nat. Catal.* **2022**, *5*, 30−36.
(35) Aran-Ais, R. M.; Rizo, R.; Grosse, P.; Algara-Siller, G.; Dembele, K.; Plodinec, M.; Lunkenbein, T.; Chee, S. W.; Cuenya, B. R. Imaging Electrochemically Synthesized Cu_2O Cubes and Their Morphological Evolution under Conditions Relevant To CO_2 Electroreduction. *Nat. Commun.* **2020**, *11*, 3489.
(36) Yang, Y.; Louisia, S.; Yu, S.; Jin, J.; Roh, I.; Chen, C.; Fonseca Guzman, M. V.; Feijóo, J.; Chen, P.-C.; Wang, H.; Pollock, C. J.; Huang, X.; Shao, Y.-T.; Wang, C.; Muller, D. A.; Abruña, H. D.; Yang, P. Operando Studies Reveal Active Cu Nanograins for CO_2 Electroreduction. *Nature* **2023**, *614*, 262−269.
(37) Yang, Y.; Shi, C.; Feijóo, J.; Jin, J.; Chen, C.; Han, Y.; Yang, P. Dynamic Evolution of Copper Nanowires during CO_2 Reduction Probed by Operando Electrochemical 4D-STEM and X-ray Spectroscopy. *J. Am. Chem. Soc.* **2024**, *146*, 23398−23405.
(38) Gu, M.; Parent, L. R.; Mehdi, B. L.; Unocic, R. R.; McDowell, M. T.; Sacci, R. L.; Xu, W.; Connell, J. G.; Xu, P.; Abellan, P.; Chen, X.; Zhang, Y.; Perea, D. E.; Evans, J. E.; Lauhon, L. J.; Zhang, J. G.; Liu, J.; Browning, N. D.; Cui, Y.; Arslan, I.; Wang, C. M. Demonstration of an Electrochemical Liquid Cell for Operando Transmission Electron Microscopy Observation of the Lithiation/Delithiation Behavior of Si Nanowire Battery Anodes. *Nano Lett.* **2013**, *13*, 6106−6112.
(39) Holtz, M. E.; Yu, Y.; Gunceler, D.; Gao, J.; Sundararaman, R.; Schwarz, K. A.; Arias, T. A.; Abruña, H. D.; Muller, D. A. Nanoscale Imaging of Lithium Ion Distribution during In Situ Operation of Battery Electrode and Electrolyte. *Nano Lett.* **2014**, *14*, 1453−1459.
(40) Zeng, Z.; Zhang, X.; Bustillo, K.; Niu, K.; Gammer, C.; Xu, J.; Zheng, H. In Situ Study of Lithiation and Delithiation of MoS_2 Nanosheets Using Electrochemical Liquid Cell Transmission Electron Microscopy. *Nano Lett.* **2015**, *15*, 5214−5220.
(41) Sacci, R. L.; Black, J. M.; Balke, N.; Dudney, N. J.; More, K. L.; Unocic, R. R. Nanoscale Imaging of Fundamental Li Battery Chemistry: Solid-Electrolyte Interphase Formation and Preferential Growth of Lithium Metal Nanoclusters. *Nano Lett.* **2015**, *15*, 2011−2018.
(42) Park, H.; Jeon, Y.; Chung, W. J.; Bae, Y.; Kim, J.; Baek, H.; Park, J. Early Stage Li Plating by Liquid Phase and Cryogenic Transmission Electron Microscopy. *ACS Energy Lett.* **2023**, *8*, 715−721.
(43) Vance, J. R.; Dillon, S. J. Thermally Driven Bubble Evolution at a Heater Wire in Water Characterized by High-Speed Transmission Electron Microscopy. *Chem. Commun.* **2017**, *53*, 4930−4933.
(44) Tan, S. F.; Bisht, G.; Anand, U.; Bosman, M.; Yong, X. E.; Mirsaidov, U. In Situ Kinetic and Thermodynamic Growth Control of Au-Pd Core-Shell Nanoparticles. *J. Am. Chem. Soc.* **2018**, *140*, 11680−11685.
(45) Khelfa, A.; Nelayah, J.; Amara, H.; Wang, G.; Ricolleau, C.; Alloyeau, D. Quantitative In Situ Visualization of Thermal Effects on the Formation of Gold Nanocrystals in Solution. *Adv. Mater.* **2021**, *33*, 2102514.
(46) Lee, S.; Schneider, N. M.; Tan, S. F.; Ross, F. M. Temperature Dependent Nanochemistry and Growth Kinetics Using Liquid Cell Transmission Electron Microscopy. *ACS Nano* **2023**, *17*, 5609−5619.
(47) van Omme, J. T.; Wu, H.; Sun, H.; Beker, A. F.; Lemang, M.; Spruit, R. G.; Maddala, S. P.; Rakowski, A.; Friedrich, H.; Patterson, J. P.; Perez Garza, H. H. Liquid Phase Transmission Electron Microscopy with Flow and Temperature Control. *J. Mater. Chem. C* **2020**, *8*, 10781−10790.
(48) Korpanty, J.; Wang, C.; Gianneschi, N. C. Upper Critical Solution Temperature Polymer Assemblies Via Variable Temperature Liquid Phase Transmission Electron Microscopy and Liquid Resonant Soft X-Ray Scattering. *Nat. Commun.* **2023**, *14*, 3441.
(49) Tan, S. F.; Reidy, K.; Klein, J.; Pinkowitz, A.; Wang, B.; Ross, F. M. Real-Time Imaging of Nanoscale Electrochemical Ni Etching under Thermal Conditions. *Chem. Sci.* **2021**, *12*, 5259−5268.

https://doi.org/10.1021/jacs.5c05005
J. Am. Chem. Soc. XXXX, XXX, XXX−XXX

(50) Rosenberg, R.; Edelstein, D. C.; Hu, C.-K.; Rodbell, K. P. Copper Metallization for High Performance Silicon Technology. *Annu. Rev. Mater. Sci.* **2000**, *30*, 229−262.
(51) *Adsorption on Metal Surfaces*, Bénard, J., Ed.; Elsevier: Amsterdam, 1983
(52) Holtz, M. E.; Yu, Y.; Gao, J.; Abruña, H. D.; Muller, D. A. In Situ Electron Energy-Loss Spectroscopy in Liquids. *Microsc. Microanal.* **2013**, *19*, 1027−1035.
(53) Yang, Y.; Roh, I.; Louisia, S.; Chen, C.; Jin, J.; Yu, S.; Salmeron, M. B.; Wang, C.; Yang, P. Operando Resonant Soft X-Ray Scattering Studies of Chemical Environment and Interparticle Dynamics of Cu Nanocatalysts for CO_2 Electroreduction. *J. Am. Chem. Soc.* **2022**, *144*, 8927−8931.
(54) Bard, A. J.; Faulkner, L. R.; White, H. *Electrochemical Methods: Fundamental and Applications, 3rd Ed.*; John Wiley & Sons: Hoboken, NJ, 2022; p 323.
(55) Yang, Y.; Shao, Y.-T.; DiSalvo, F. J.; Muller, D. A.; Abruña, H. D. Metal Monolayers on Command: Underpotential Deposition at Nanocrystal Surfaces: A Quantitative Operando Electrochemical Transmission Electron Microscopy Study. *ACS Energy Lett.* **2022**, *7*, 1292−1297.
(56) Schneider, N. M.; Park, J. H.; Grogan, J. M.; Steingart, D. A.; Bau, H. H.; Ross, F. M. Nanoscale Evolution of Interface Morphology during Electrodeposition. *Nat. Commun.* **2017**, *8*, 2174.
(57) Kirkland, E. J. *Advanced Computing in Electron Microscopy*, 2nd ed., Springer: New York, 2009; p 107.
(58) Ercius, P.; Muller, D. Incoherent Bright Field STEM for Imaging and Tomography of Ultra-Thick TEM Cross-Sections. *Microsc. Microanal.* **2009**, *15*, 238−239.
(59) Ercius, P.; Weyland, M.; Muller, D. A.; Gignac, L. M. Three-dimensional imaging of nanovoids in copper interconnects using incoherent bright field tomography. *Appl. Phys. Lett.* **2006**, *88*, 243116.
(60) Tonietto, L.; Gonzaga, L.; Veronez, M. R.; Kazmierczak, C. d. S.; Arnold, D. C. M.; Costa, C. A. d. New Method for Evaluating Surface Roughness Parameters Acquired by Laser Scanning. *Sci. Rep.* **2019**, *9*, 15038.
(61) Qiao, X.; Li, H.; Zhao, W.; Li, D. Effects of Deposition Temperature on Electrodeposition of Zinc-nickel Alloy Coatings. *Electrochim. Acta* **2013**, *89*, 771−777.
(62) Yan, K.; Wang, J.; Zhao, S.; Zhou, D.; Sun, B.; Cui, Y.; Wang, G. Temperature-Dependent Nucleation and Growth of Dendrite-Free Lithium Metal Anodes. *Angew. Chem., Int. Ed.* **2019**, *58*, 11364−11490.
(63) Buzzeo, M. C.; Hardacre, C.; Compton, R. G. Extended Electrochemical Windows Made Accessible by Room Temperature Ionic Liquid/Organic Solvent Electrolyte Systems. *ChemPhysChem* **2006**, *7*, 176−180.
(64) Brady, R. M.; Ball, R. C. Fractal Growth of Copper Electrodeposits. *Nature* **1984**, *309*, 225−229.
(65) Wang, X.; Zeng, W.; Hong, L.; Xu, W.; Yang, H.; Wang, F.; Duan, H.; Tang, M.; Jiang, H. Stress-Driven Lithium Dendrite Growth Mechanism and Dendrite Mitigation by Electroplating on Soft Substrates. *Nat. Energy* **2018**, *3*, 227−235.
(66) Nishikawa, K.; Chassaing, E.; Rosso, M. Evolution of the Morphology of Electrodeposited Copper at the Early Stage of Dendritic Growth. *J. Electrochem. Soc.* **2013**, *160*, D183−D187.
(67) Xia, X.; Xie, S.; Liu, M.; Peng, H.-C.; Lu, N.; Wang, J.; Kim, M. J.; Xia, Y. On the Role of Surface Diffusion in Determining the Shape or Morphology of Noble-Metal Nanocrystals. *Proc. Natl. Acad. Sci. U.S.A.* **2013**, *110*, 6669−6673.
(68) Zhang, Y.; Li, Y.; Shen, W.; Li, K.; Lin, Y. Important Role of Atom Diffusion in Dendrite Growth and the Thermal Self-Healing Mechanism. *ACS Appl. Energy Mater.* **2023**, *6*, 1933−1945.
(69) Grujicic, D.; Pesic, B. Electrodeposition of copper: The nucleation mechanisms. *Electrochim. Acta* **2002**, *47*, 2901−2912.
(70) Guo, Y.; Li, D.; Xiong, R.; Li, H. Investigation of the temperature-dependent behaviors of Li metal anode. *Chem. Commun.* **2019**, *55*, 9773−9776.
(71) Xu, X.; Liu, Y.; Hwang, J.-Y.; Kapitanova, O. O.; Song, Z.; Sun, Y.-K.; Matic, A.; Xiong, S. Role of Li-Ion Depletion on Electrode Surface: Underlying Mechanism for Electrodeposition Behavior of Lithium Metal Anode. *Adv. Energy Mater.* **2020**, *10*, 2002390.
(72) Yan, H. H.; Bie, Y. H.; Cui, X. Y.; Xiong, G. P.; Chen, L. A Computational Investigation of Thermal Effect on Lithium Dendrite Growth. *Energy Convers. Manag.* **2018**, *161*, 193−204.
(73) Bai, P.; Li, J.; Brushett, F. R.; Bazant, M. Z. Transition of Lithium Growth Mechanisms in Liquid Electrolytes. *Energy Environ. Sci.* **2016**, *9*, 3221−3229.
(74) Yu, S.-H.; Huang, X.; Brock, J. D.; Abruña, H. c. D. Regulating Key Variables and Visualizing Lithium Dendrite Growth: An Operando X-ray Study. *J. Am. Chem. Soc.* **2019**, *141*, 8441−8449.
(75) Yang, Y.; Shao, Y.-T.; Lu, X.; Yang, Y.; Ko, H.-Y.; DiStasio, R. A.; DiSalvo, F. J.; Muller, D. A.; Abruña, H. D. Elucidating Cathodic Corrosion Mechanisms with Operando Electrochemical Transmission Electron Microscopy. *J. Am. Chem. Soc.* **2022**, *144*, 15698−15708.
(76) Yang, Y.; Shao, Y.-T.; Jin, J.; Feijóo, J.; Roh, I.; Louisia, S.; Yu, S.; Fonseca Guzman, M. V.; Chen, C.; Muller, D. A.; Abruña, H. D.; Yang, P. Operando Electrochemical Liquid-Cell Scanning Transmission Electron Microscopy (EC-STEM) Studies of Evolving Cu Nanocatalysts for CO_2 Electroreduction. *ACS Sustain. Chem. Eng.* **2023**, *11*, 4119−4124.
(77) Tate, M. W.; Purohit, P.; Chamberlain, D.; Nguyen, K. X.; Hovden, R.; Chang, C. S.; Deb, P.; Turgut, E.; Heron, J. T.; Schlom, D. G.; Ralph, D.; Fuchs, G. D.; Shanks, K. S.; Philipp, H. T.; Muller, D. A.; Gruner, S. M. High Dynamic Range Pixel Array Detector for Scanning Transmission Electron Microscopy. *Microsc. Microanal.* **2016**, *22*, 237−249.
(78) Chen, Z.; Jiang, Y.; Shao, Y.-T.; Holtz, M. E.; Odstrcil, M.; Guizar-Sicairos, M.; Hanke, I.; Ganschow, S.; Schlom, D. G.; Muller, D. A. Electron Ptychography Achieves Atomic-Resolution Limits Set by Lattice Vibrations. *Science* **2021**, *372*, 826−831.
(79) Hartigan, J. A.; Wong, M. A. A K-means Clustering Algorithm. *J. Roy. Stat. Soc. C Appl. Stat.* **1979**, *28*, 100−108.
(80) Shi, C.; Cao, M. C.; Rehn, S. M.; Bae, S. H.; Kim, J.; Jones, M. R.; Muller, D. A.; Han, Y. Uncovering Material Deformations via Machine Learning Combined with Four-Dimensional Scanning Transmission Electron Microscopy. *npj Comput. Mater.* **2022**, *8*, 114.
(81) Shi, C.; Cheng, Z.; Leonardi, A.; Yang, Y.; Engel, M.; Jones, M. R.; Han, Y. Preserving Surface Strain in Nanocatalysts via Morphology Control. *Sci. Adv.* **2024**, *10*, adp378.
(82) Li, F.; Medvedeva, X. V.; Medvedev, J. J.; Khairullina, E.; Engelhardt, H.; Chandrasekar, S.; Guo, Y.; Jin, J.; Lee, A.; Thérien-Aubin, H.; Ahmed, A.; Pang, Y.; Klinkova, A.; Klinkova, A. Interplay of electrochemical and electrical effects induces structural transformations in electrocatalysts. *Nat. Catal.* **2021**, *4*, 479−487.
(83) Gaspari, G.; Cohn, S. E. Construction of correlation functions in two and three dimensions. *Q. J. R. Meteorol. Soc.* **1999**, *125*, 723−757.
(84) de Bethune, A. J.; Licht, T. S.; Swendeman, N. The Temperature Coefficients of Electrode Potentials. *J. Electrochem. Soc.* **1959**, *106*, 616−624.
(85) Bard, A. J.; Parson, R.; Jordan, J. *Standard Potentials in Aqueous Solution*; Marcel Dekker, Inc., 1985.
(86) Greeley, R. S.; Smith, W. T.; Stoughton, R. W.; Lietzke, M. H. Electromotive Force Studies in Aqueous Solutions at Elevated Temperatures. I. The Standard Potential of the Silver-Silver Chloride Electrode. *J. Phys. Chem.* **1960**, *64*, 652−657.
(87) Yang, Y.; Agarwal, R. G.; Hutchison, P.; Rizo, R.; Soudackov, A. V.; Lu, X.; Herrero, E.; Feliu, J. M.; Hammes-Schiffer, S.; Mayer, J. M.; Abruña, H. D. Inverse Kinetic Isotope Effects in the Oxygen Reduction Reaction at Platinum Single Crystals. *Nat. Chem.* **2023**, *15*, 271−277.
(88) Schneider, N. M.; Norton, M. M.; Mendel, B. J.; Grogan, J. M.; Ross, F. M.; Bau, H. H. Electron-Water Interactions and Implications for Liquid Cell Electron Microscopy. *J. Phys. Chem. C* **2014**, *118*, 22373−22382.
(89) Fritsch, B.; Hutzler, A.; Wu, M.; Khadivianazar, S.; Vogl, L.; Jank, M. P. M.; Marz, M.; Spiecker, E. Accessing Local Electron-Beam Induced Temperature Changes During In Situ Liquid-Phase Transmission Electron Microscopy. *Nanoscale Adv.* **2021**, *3*, 2466−2474.

https://doi.org/10.1021/jacs.5c05005
J. Am. Chem. Soc. XXXX, XXX, XXX−XXX

(90) Ambrožič, B.; Prašnikar, A.; Hodnik, N.; Kostevšek, N.; Likozar, B.; Rožman, K. Ž.; Sturm, S.; Sturm, S. Controlling the radical-induced redox chemistry inside a liquid-cell TEM. *Chem. Sci.* **2019**, *10*, 8735−8743.
(91) Philipp, H. T.; Tate, M. W.; Shanks, K. S.; Mele, L.; Peemen, M.; Dona, P.; Hartong, R.; van Veen, G.; Shao, Y.-T.; Chen, Z.; et al. Very-High Dynamic Range, 10,000 Frames/Second Pixel Array Detector for Electron Microscopy. *Microsc. Microanal.* **2022**, *28*, 425−440.

https://doi.org/10.1021/jacs.5c05005
J. Am. Chem. Soc. XXXX, XXX, XXX−XXX